A DISSERTATION FOR THE DEGREE OF PHILOSOPHIAE DOCTOR

The Protonics project: distributed observations of auroral dayside Doppler-shifted hydrogen emissions

Jeffrey Morgan Holmes

February 2014

Department of Physics, Faculty of Mathematics and Natural Sciences,
University of Oslo, Norway

in cooperation with

UNIS

Department of Arctic Geophysics
The University Centre in Svalbard, Longyearbyen, Norway

Series of dissertations submitted to the
Faculty of Mathematics and Natural Sciences, University of Oslo
No. 1529

ISSN 1501-7710

Cover: Inger Sandved Anfinsen.
Printed in Norway: AIT Oslo AS.

Produced in co-operation with Akademika Publishing.
The thesis is produced by Akademika Publishing merely in connection with the thesis defence. Kindly direct all inquiries regarding the thesis to the copyright holder or the unit which grants the doctorate.

Bring on the night
I couldn't stand another hour of daylight

– The Police, 1979

Acknowledgements

I would like to give thanks to those who I have learned a tremendous amount over the last years: my advisors Professor Dag Lorentzen and Professor Fred Sigernes. I feel very privileged to be able to refine my experimental techniques and learn the finer points of dayside aurora from both of them. From my first arctic lesson with Fred, to my first polar bear encounter with Dag, my education on Svalbard has been quite diverse. I also feel quite honoured to be a part of the team of scientists, both from The University Centre in Svalbard (UNIS) and our collaborating international institutions, that worked at the close of historic *Nordlysstasjonen* (The Auroral Station) in Adventdalen and the opening of the Kjell Henriksen Observatory (KHO).

Special thanks also go to my mentors and collaborators Dr. Boris Kozelov, Professor Charles Deehr, and Dr. Magnar Gullikstad Johnsen who have helped me tremendously. Thanks also to Mr. Matteo Ottaviani, who played a major role in the deployment of the Black spectrometer to Ny-Ålesund, which provided essential data. I would also like to acknowledge Professor Jøran Moen for being my advisor at the University of Oslo. Thanks also to Espen Trondsen for helping me in lots of different ways.

I would like to recognize and the life and work of the late Nikita Shumilov, my predecessor. I was fortunate to briefly collaborate with Nikita while living in London, but never had the privilege of meeting him in person.

Extra special thanks must go to my fellow station/observatory co-manager, Dr. Margit Dyrland. She was a great partner in managing the old station and the new observatory. Each of us probably could have managed it alone, but together our differing skills complemented each other quite well!

I would like to acknowledge and say thanks for the opportunities given to me by both Professor Mark Conde in Fairbanks, Alaska and Professor David Rees in London, England. Without their encouragement and support, I would probably never have even heard of Svalbard. A thousand thanks go to Professor Deehr for recruiting me to go to Longyearbyen in 2003 as the fill-in seasonal manager of *Nordlysstasjonen*.

In Austin, Dr. Gary Bust introduced me to both the ionosphere and scientific programming; I owe him a debt of gratitude as well. Dr. Todd Pedersen and my other new colleagues at the U.S. Air Force Research Laboratory have helped me stay motivated by teaching me plenty of new things and exposing me to fascinating new research topics, both polar- and coconut-related.

To my friends on Svalbard and the mainland, abroad, and back home who have supported me through good and bad times – especially Lisa Baddeley, Sébastien Barrault, Hanne Sigerun Byhring, Rico Behlke, Karoline Bælum, Andy Charalambous, Charles Jack Chesky, Stefan Claes, Hanna Dahlgren, Amy Denney, Yvonne and Kenneth Dåbakk, Cpt. Daniel Emmons, Tom Grydeland, Eggert Gudmundsson, Björn Gustavsson, Poul Jensen, Jörg Lenk, Sylvi Lundgren and her family, Martin Morgoth and Stine Skoglund Machiedo, Ian McWhirter, R. Todd Parris, Ragnar Ólafsson, Ketil Rønning, *Familien* Sandvik, Lt. Brett Stephens, Anja Strømme, Eric Sutton, Aaron and Jacob Taylor, Donald Thompson, Trond Trondsen, Monika Trümper, and Mea and Cyril Simon Wedlund – *tusen takk*, y'all! I must also give extra thanks to Timothy Holmes, Edward Fleissner and my extended family in Albuquerque and elsewhere.

And to those dearest to me, my mother Claire and my sister Amy: words cannot describe how I appreciate a lifetime of support and encouragement. This work is dedicated to you both.

Albuquerque, New Mexico, February 2014 Jeffrey Morgan Holmes

Abstract

The Protonics project is an effort to further understand the spatio-temporal dynamics of dayside auroral hydrogen emissions, also known as dayside proton aurorae. Spectrometers measuring dayside Balmer α (H_α) and Balmer β (H_β) were deployed to two locations on Svalbard at Longyearbyen and Ny-Ålesund. Measured hydrogen Doppler profiles were analysed via a Monte Carlo model of proton precipitation, resulting in an estimate of characteristic energy of the precipitating proton/hydrogen population. The difference in energy found between the two stations is interpreted as an ionospheric signature of magnetic merging near the magnetopause.

Initially, a significant energy difference was discovered in two cases. However, weak emissions required spectral scans from the two instruments to be separately averaged for roughly two hours to produce the result. A third case featuring a stronger proton precipitation event was found, resulting in a statistically significant difference in energy with averaging on the order of minutes. This third case is the first statistically significant ground-based detection of the ion velocity filter effect in the dayside hydrogen aurora.

A natural extension of the project was to investigate the relative occurrence of electron and proton aurora under the influence of solar wind shocks across the boreal auroral zone. Since this study required areal data coverage much larger than the vicinity of Svalbard, data from meridian scanning photometers (MSP) in Canada, Greenland and Svalbard were combined and compared with large-scale UV auroral images from the Polar spacecraft. Analysis of MSP data for events previously studied solely using space-based imagery added needed spatio-temporal resolution. Shock aurora propagation times were refined, and agreed with previous results to within uncertainties. Furthermore, the majority of instruments detected low energy discrete auroral arcs poleward of diffuse, higher energy proton and electron aurora. Two-pulse proton aurora onset sequences were also observed.

A significant amount of time and effort was spent to ensure that the ground-based instruments had correct wavelength and intensity calibrations; the methodology for calibrating with respect to both is discussed in detail. Finally, the growing importance of inexpensive, commercially available digital single lens reflex cameras was recognized, and a detailed scheme for intensity calibration of the individual colours of a camera's detector is described. Such instruments have proven quite useful as auroral context instruments and cloud detectors, thereby reducing time and effort required for data reduction.

Preface

This dissertation is primarily concerned with the study of Doppler-shifted hydrogen emissions occurring in the lower thermosphere – dayside proton aurorae. In addition, a study of relative proton and electron auroral propagation under the influence of solar wind interplanetary shocks was performed using distributed instruments in the North American and Scandinavian sectors. A significant amount of work was also done with the calibration of various optical instruments used to acquire such data.

The majority of this work took place in cooperation with the University Centre on Svalbard (UNIS), through which I received funding to pursue my dissertation research. Data presented herein were largely acquired at *Nordlysstasjonen* (The Auroral Station) in Adventdalen during the final seasons of its operation before being succeeded by the Kjell Henriksen Observatory (KHO).

In addition to the papers presented, I contributed to other research endeavours resulting in the following publications:

C. Simon, J. Lilensten, J. Moen, J. M. Holmes, Y. Ogawa, K. Oksavik, and W. F. Denig (2007), TRANS4: a new coupled electron/proton transport code – comparison to observations above Svalbard using ESR, DMSP and optical measurements, *Ann. Geo., 25*, 661-673.

Lorentzen, D. A., P. M. Kintner, J. Moen, F. Sigernes, K. Oksavik, Y. Ogawa, and J. M. Holmes (2007), Pulsating dayside aurora in relation to ion upflow events during a northward IMF dominated by a strongly negative IMF B_y, *J. Geophys. Res., 112*, A03301, doi:10.1029/2006JA011757.

Kozelov, B. V. and J. M. Holmes (2008), Angle scattering and forming the hydrogen Doppler profile in proton aurora, "Physics of Auroral Phenomena", *Proc. XXXI Annual Seminar*, Apatity, Kola Science Centre, Russian Academy of Sciences, 153-156.

Johnsen, M. G., D. A. Lorentzen, J. M. Holmes, and U. P. Løvhaug (2012), A model based method for obtaining the open/closed field line boundary from the cusp auroral 6300 Å [OI] red line, *J. Geophys. Res.*, 117, A03319, doi:10.1029/2011JA016980.

The organization of this work is as follows: An introduction is given in Section 1, including fundamentals of radiometric calibration of optical instruments, history, theory and recent advances in proton aurora research, and a review of aurora occurring under the

influence of solar wind shocks, known as shock aurora. Motivation for the research undertaken is presented in Section 2. A summary of the papers comprising the effort is found in Section 3. A review of current outstanding problems and potential future research topics is in Section 4, with references for all of the above in Section 5. Five papers on the previously introduced topics conclude the work.

Contents

Abstract vii

Preface ix

Contents xi

1. Introduction 1

1.1 Radiometric calibration of optical instruments 1

1.1.1. Fundamental radiometric concepts 1

1.1.2. The Rayleigh 2

1.1.3. Laboratory and vicarious calibration of aeronomic optical instruments 4

1.1.4. Calibration of digital single lens reflex cameras and their applications in aeronomy 10

1.2. Proton aurora 14

1.2.1. Hydrogen spectra and thermospheric proton precipitation 15

1.2.1.1 Discovery and phenomenology 15

1.2.1.2 Recent theoretical and observational advances 17

1.2.2. Dayside proton aurora as a visible tracer of magnetopause boundary layer dynamics 22

1.3. Proton and electron shock aurora 26

2. Motivation 29

3. Summary of papers 33

4. Outstanding Problems and Future Work 37

5. References 39

Paper I - Sigernes, F., J. M. Holmes, M. Dyrland, D. Lorentzen, S. Chernous, T. Svenøe, J. Moen, and C. S. Deehr (2007), Absolute calibration of optical devices with a small field of view, *J. Opt. Technol.*, *74,* 669-674. 49

Paper II - Sigernes, F., J. M. Holmes, M. Dyrland, D. A. Lorentzen, T. Svenøe, K. Heia, T. Aso, S. Chernouss, and C. S. Deehr (2008), Sensitivity calibration of digital colour cameras for auroral imaging, *Opt. Express, 16*, 15623-15632. 63

Paper III - Holmes, J. M., B. V. Kozelov, F. Sigernes, D. A. Lorentzen, and C. S. Deehr, Dual site observations of dayside Doppler-shifted hydrogen profiles: preliminary results. *Can. J. Phys.*, *86*(5): 691–698 (2008), doi:10.1139/P08-026. 77

Paper IV - Holmes, J. M., B. V. Kozelov, N. J. Peters, C. S. Deehr, D. A. Lorentzen, 95

and F. Sigernes (2009), Ion velocity filter effect observed in dayside hydrogen aurora, *Geophys. Res. Lett.*, *36*, L23101, doi:10.1029/2009GL040972.

Paper V - Holmes, J. M., M. G. Johnsen, C. S. Deehr, X.-Y Zhou, and D. A. Lorentzen (2014), Circumpolar ground-based optical measurements of proton and electron shock aurora, *J. Geophys. Res. Space Physics, 119,* 3895–3914, doi:10.1002/2013JA019574. 109

1. Introduction

1.1. Radiometric calibration of optical instruments

In the modern paradigm, radiometry is the study of the measurement of optical electromagnetic fields in the frequency range $3\text{x}10^{11}$ – $3\text{x}10^{16}$ Hz (λ1000 μm – 10 nm). More specifically, it deals with the energy content of electromagnetic radiation and how it is transmitted from a source to a detector via a medium [*Bass et al*., 2005].

The scope of the following sections will be limited to radiometric treatment of visible and near-infrared wavelengths from 400 nm, the approximate blue limit of the human eye, to 1000 nm, the red limit of silicon detectors. Furthermore, the formalism that is used makes basic assumptions, namely that light propagation can be fully realized with geometric optics, the medium is lossless, and that diffraction and interference effects can be neglected. The degree of source coherence is also ignored. Rigorous treatises on radiometry can be found by, e.g., *Wyatt* [1978]; *Boyd* [1983]; *Pamler and Grant* [2009].

1.1.1. Fundamental radiometric concepts

In order to depict clearly how aeronomic optical instruments are calibrated, it is important to describe the fundamental radiometric quantities used and their units. In this section, SI units will be used exclusively. The section that follows will introduce the Rayleigh, a unit used in aeronomical and astronomical community, and the conversions to and from SI.

There are three quantities that characterize an observing or calibration setup, comprised of a source, a medium (including any instrumental optics), and a detector. All three are geometric variations on the *radiant power* of electromagnetic radiation. When considering the total power emanating from or received at a point source, the radiant power Φ can be expressed as:

$$\Phi = \frac{dQ}{dt} \quad \left[\frac{J}{s}\right], \left[W\right], \text{ or } \left[\frac{photons}{s}\right], \tag{1}$$

where Q is the radiant energy emitted or received.

Irradiance, E, is defined as the ratio of radiant power incident upon a surface element dA to its projected area. With ϕ being the angle between the surface normal and the direction of radiation, irradiance can be expressed in terms of radiant power per unit area:

$$E \equiv \frac{d\Phi}{dA\cos\phi} \quad \left[\frac{photons}{s \cdot m^2}\right]. \tag{2}$$

Note that the term *exitance* (denoted by *M*) is mathematically identical to irradiance, except that this nomenclature is used to describe the radiant power per unit area *emitted* from a surface. Useful geometrical relationships for discussing irradiance and exitance are shown in Figure 1.

Radiant *intensity* describes the ratio of power to unit solid angle in a given direction. It applies to the power per solid angle, Ω, both incident upon and emanating from a point. Denoted by I, it is expressed simply as:

$$I \equiv \frac{d\Phi}{d\Omega} \quad \left[\frac{photons}{s \cdot sr}\right]. \tag{3}$$

Finally, the ratio of radiant power at an angle ϕ to an infinitesimal projected area and solid angle is the *radiance, L*:

$$L \equiv \frac{d\Phi}{dAd\Omega\cos\phi} \quad \left[\frac{photons}{s \cdot m^2 \cdot sr}\right]. \tag{4}$$

Radiance is important since in an idealized (i.e. lossless) system, it is the parameter that is conserved. In the sections that follow, concepts of irradiance, intensity and radiance will be applied to a practical calibration experiment, comprised of an emitting screen as a source and a photometer or Charge Coupled Device (CCD) based instrument as the detector.

1.1.2. The Rayleigh

The Fourth Baron Rayleigh, Robert John Strutt, was the first to make absolute measurements of the night airglow intensity [*Rayleigh*, 1930]. The aeronomical community adopted the unit bearing his name after introduction by *Hunten et al*. [1956], later reinforced by *Chamberlain* [1961]. They conceived the unit specifically to describe the integrated column emission rate of a distant source, with units of *photons* s^{-1} m^{-2} col^{-1}. (Note that 'col' was included in the specification of the units to distinguish a column-

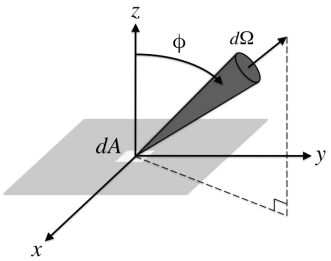

Figure 1. Relationship between infinitesimal quantities of area dA and directed solid angle $d\Omega$.

-integrated volume emission rate from a general photon fluence of identical dimensions.) The Rayleigh, R, was historically defined as a *megaphoton cm^{-2} column^{-1} s^{-1}*. In SI units:

$$R \equiv \frac{10^{10}\, photons}{s \cdot \left(m^2 \cdot col\right)}. \tag{5}$$

This measure of the line-of-sight integrated volume emission rate is quite useful for extended sources that are optically thin (i.e. negligible scattering or re-absorption), such as auroral and airglow investigations, as exemplified below.

Given that upper atmospheric emission sources radiate based on the local physical constraints and without any regard to the line of sight of a remote observer, a method of converting Rayleighs measured from the ground or space to the above mentioned fundamental radiometric units is required. As discussed by *Chamberlain* [1961] and more explicitly in *Baker and Romick* [1976], the Rayleigh can be interpreted directly and more generally as a measure of photon radiance. This interpretation precludes the need to make *a priori* assumptions about the nature of the radiating medium or radiative transfer requirements between the source and the detector (e.g., how it is distributed along the line of sight, whether it is emitting isotropically, etc.). The generalized definition of the Rayleigh is:

$$R \equiv \frac{1}{4\pi} \frac{10^{10}\, photons}{s \cdot \left(m^2 \cdot sr\right)}. \tag{6}$$

It is constructive to show examples of how to apply each of the two formulations of the Rayleigh. If one considers an auroral feature or airglow layer of thickness H and wavelength λ along an observer's line of sight measured to be an irradiance of E_λ Rayleighs, (5) is used to calculate the average volume emission rate over the column, $\bar{\eta}_\lambda$:

$$\bar{\eta}_\lambda \left[\frac{10^{10}\, photons}{s \cdot m^3 \cdot nm} \right] = E_\lambda \left[\frac{10^{10}\, photons}{s \cdot \left(m^2 \cdot col\right) \cdot nm} \right] \times \frac{1}{H} \left[\frac{col}{m} \right]. \tag{7}$$

The directional volume emission rate distribution of the source can be found by dividing (7) by 4π steradians.

The generalized definition of the Rayleigh is applied in the second example, considering the laboratory calibration of an instrument using a diffusing screen. A flat diffusor is defined to be Lambertian if the radiance is independent of viewing angle. Equivalently, the radiant intensity varies as the cosine of the viewing angle relative to the surface normal. This is known as Lambert's Cosine Law [*Lambert*, 1760]. Consider a

detector of area a measuring L_λ Rayleighs, while its field of view (FOV) is fully filled by a uniformly illuminated, Lambertian screen. The intensity of the radiation received at the detector is then:

$$I_\lambda\left[\frac{photons}{s\cdot sr\cdot nm}\right]=L_\lambda\left[\frac{photons}{s\cdot\left(m^2\cdot sr\right)\cdot nm}\right]\times a\left[m^2\right]. \tag{8}$$

Given the Lambertian property of the screen, the radiant power can be found by multiplying by the 2π steradians in the reflecting hemisphere:

$$\Phi_\lambda\left[\frac{photons}{s\cdot nm}\right]=I_\lambda\left[\frac{photons}{s\cdot sr\cdot nm}\right]\times 2\pi\left[sr\right]. \tag{9}$$

Considering the dual interpretation of the Rayleigh, one as a measure of the column-integrated volume emission rate and the other of radiance, it is clear that the calibration of optical instrumentation used to observe atmospheric emissions is conveniently done using the Rayleigh. A practical description of such calibration experiments follows in the next section.

1.1.3. Laboratory and vicarious calibration of aeronomic optical instruments

Generally, a calibration scheme is a method to relate quanta measured by an instrument to known physical quantities. For example, optical calibration of instruments can take the form of converting photometer pulses in voltage or discrete digital counts in a CCD to a radiance in Rayleighs or $mW\cdot m^{-2}\cdot sr^{-1}$. This process essentially results in a multiplicative calibration factor that relates the number of counts or pulses registered by a data acquisition system to the number of input photons.

Calibration lamps are commonly used as sources of known radiance (or irradiance). The calibration facility at UNIS uses tungsten lamps that are traceable back to the U.S. National Institute of Standards and Technology. Each is paired with an official tabulation of the lamp irradiance as a function of wavelength, both in *photons* m^{-2} s^{-1} nm^{-1} and mW m^{-2} nm^{-1}, known as the lamp *certificate*. Measured and certified at an exact distance of z_0 = 1 m, $B_{0\lambda}$ is the known irradiance.

In addition, since view angles of real instruments are not infinitesimally narrow and the detectors used are not point-detectors, some apparatus is required that will evenly distribute the radiance of the lamp over the instrument's field of view. While many approaches are possible, the UNIS calibration laboratory features both a flat diffusor screen and an integrating sphere. For simplicity, the formulation that follows will feature a Lambertian

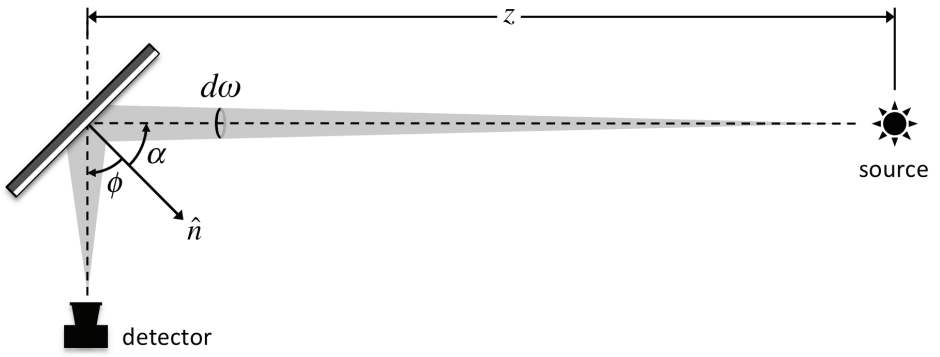

Figure 2. Idealized calibration setup comprised of a source, diffusor screen, and a detector.

diffusor screen; the method can be adapted for the use of a sphere.

A flat surface that is uniformly emitting or reflecting, when observed from an angle ϕ to the surface normal, has a radiant intensity of

$$I_{\lambda\phi} = I_{\lambda 0}\cos\phi \quad \left[\frac{photons}{s\cdot sr\cdot nm}\right], \tag{10}$$

where $I_{\lambda 0}$ is a normalization factor representing the intensity at normal incidence. Note that for consistency with Section 1.1.1, intensity is denoted I, while R is used in Paper I. Depicted in Figure 2, for a given infinitesimal wavelength interval $d\lambda$ and solid angle $d\omega$, the flux of photons incident upon an element of the screen dA is

$$I_{s\lambda}d\omega d\lambda = I_{s\lambda}d\lambda\left(\frac{dA\cos\alpha}{z^2}\right) \quad \left[\frac{photons}{s\cdot nm}\right], \tag{11}$$

where $I_{s\lambda}$ is the intensity incident upon the screen, and z is the distance from the source to the screen. Assuming a reflectance coefficient of ρ_λ ($\cong 0.98$), the screen's reflected photon flux is

$$\rho_\lambda\left\{I_{s\lambda}d\lambda\left(\frac{dA\cos\alpha}{z^2}\right)\right\} = \pi I_{\lambda 0}d\lambda \quad \left[\frac{photons}{s\cdot nm}\right], \tag{12}$$

with the factor of π being the result of integrating (10) over the diffusing hemisphere. Equation 12 can be inserted into (10) to find the radiant intensity reflected by the screen:

$$I_{\lambda\phi} = \rho_\lambda\frac{I_{s\lambda}}{\pi}\frac{dA\cos\alpha}{z^2}\cos\phi \quad \left[\frac{photons}{s\cdot sr\cdot nm}\right], \tag{13}$$

The radiant intensity in (13) divided by the projected area of the screen as viewed from the detector is the radiance received:

$$L_\lambda = \frac{I_{\lambda\phi}}{dA\cos\phi} = \frac{1}{dA\cos\phi}\rho_\lambda\left(\frac{I_{s\lambda}}{\pi}\right)\left(\frac{dA\cos\alpha}{z^2}\right)\cos\phi$$

$$L_\lambda = \rho_\lambda\left(\frac{I_{s\lambda}}{\pi}\right)\left(\frac{\cos\alpha}{z^2}\right) \qquad \left[\frac{photons}{s\cdot sr\cdot m^3\cdot nm}\right] \tag{14}$$

Note that $dA\cos\phi$ no longer appears in the equation; only the lamp-screen distance and the angle between the lamp and the screen normal are needed. The detector-screen distance also does not matter, provided that the diffuse re-emitting screen fills the detector field of view. This is important for the vicarious calibration procedure to be discussed later.

Returning to the lamp certificate, the known irradiance $B_{0\lambda}$ can be related to both the radiant intensity and radiance emanating from the screen. Assuming the lamp radiates isotropically and losses can be neglected, the photon fluence through a sphere of radius z is identical to that of a sphere at the certification distance z_0:

$$4\pi B_{0\lambda} z_0^2 = 4\pi E_{z\lambda} z^2 . \tag{15}$$

Thus, the radiant intensity incident upon the screen can be expressed in terms of the above equation:

$$I_{s\lambda} = E_{z\lambda} z^2 = B_{0\lambda} z_0^2 . \tag{16}$$

Substituting (16) into the intensity in (14) and integrating over the reflecting hemisphere results in the radiant exitance, M_λ, leaving the screen:

$$M_\lambda = \pi L_\lambda = B_{0\lambda}\rho_\lambda\left(\frac{z_0}{z}\right)^2\cos\alpha \qquad \left[\frac{photons}{s\cdot m^2\cdot nm}\right]. \tag{17}$$

Using the historical definition, M_λ can be equivalently expressed in Rayleighs. Therefore, the ratio of M_λ to the count rate $N_{\lambda cts}$ [*counts* s^{-1}] measured by the instrument during the calibration defines the calibration factor, C_λ:

$$C_\lambda = \frac{M_\lambda}{N_{\lambda cts}} = 10^{-10}\,\frac{B_{0\lambda}\rho_\lambda\left(z_0/z\right)^2\cos\alpha}{N_{\lambda cts}} \qquad \left[\frac{R/nm}{cts/s}\right], \tag{18}$$

where the factor of 10^{-10} is needed when $B_{0\lambda}$ is known in *photons* m^{-2} s^{-1} nm^{-1}. The above factor is appropriate for an instrument such as a spectrometer or spectrograph, whose acquired data are functions of wavelength. For an imager or other instrument that acquires data averaged over some wavelength interval, C_λ can be integrated appropriately. For example, for a device using bandpass filters, the convention to determine C is to simply multiply C_λ by the full width at half maximum (FWHM) bandpass of the filter. More details of the laboratory calibration process and examples are found in Paper I.

Some differences between calibration procedures in a laboratory and those done vicariously should be noted. In this sense, vicarious calibration indicates a calibration method and environment different from the way the instrument calibration was initially performed. This can be thought of as a "field calibration", since the instrument is calibrated exactly how it is deployed. For such optical instruments on Svalbard, the environments they operate in are somewhat different from a controlled laboratory setting.

A good optical calibration laboratory allows explicit control on the environment: room temperature, humidity and lighting (or lack thereof), and so forth. Furthermore, angles, distances and other important factors are determined with more repeatability in such a setting. If possible, repeated calibrations of optical instruments in the laboratory are important to determine how various aspects of both the calibration implements, such as the lamp and diffusor screen, and the instrument itself vary with time. Examples of instrumental changes include the reduction in sensitivity of a photomultiplier tube due to seasons of light exposure, the change of bandpass and/or transmission of an interference filter, and the reduction of instrument fidelity owing to dust, moisture, repeated movements, and general wear and tear. However, owing to the high sensitivity of some instruments, moving them back into the laboratory after they have been deployed and carefully aligned is not an option.

While not a replacement for careful laboratory measurements, vicarious calibration has the distinct advantage of allowing the instrument to acquire calibration data in nearly the exact configuration that it acquires atmospheric data. In addition, since most instruments reside under transparent hemispheric domes, inclusion of the dome as an optic that is part of the instrument is necessary for a realistic calibration. Estimates of dome transmission in the visible wavelengths can be made, and have been done during the inaugural season of the Kjell Henriksen Observatory (KHO). The mean transmission from 400–700 nm for new Lexan® (polycarbonate resin thermoplastic) domes was found to be 96% [*Peters,* 2009]. Note that dome transmission after many seasons begins to degrade, presumably owing to UV exposure; scientists have noted a 'yellowing' of domes, indicating that the reduction in transmission is not uniform throughout the visible wavelength range.

The calibration scheme that UNIS employed at *Nordlysstasjonen* is identical in nature to that currently used at KHO, as depicted in Figure 3. Generally following Figure 2, the instrument to be calibrated has its field of view filled by a diffusing screen, which reflects light from the distant lamp. The current convention is to have the angle of the screen

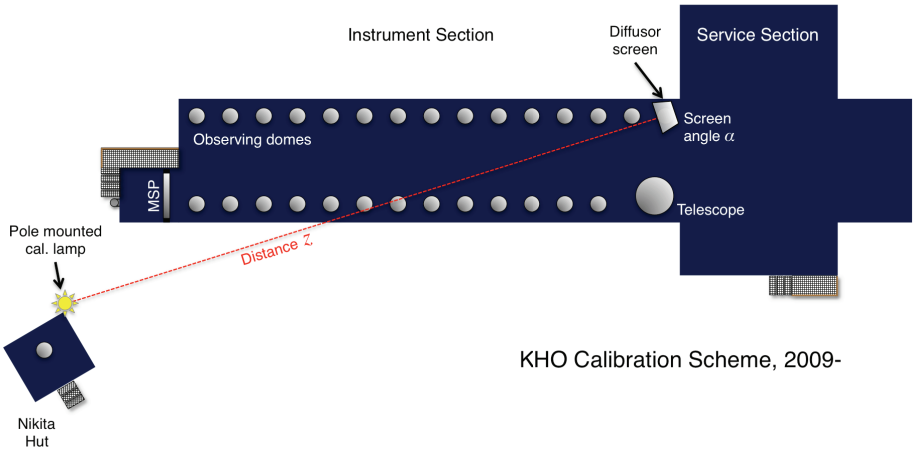

Figure 3. Vicarious calibration scheme for narrow field of view instruments at KHO. The distance from the screen to the lamp is ~50 m.

normal (α) relative to the lamp-screen axis be around 45°. Again, the angle between the screen and instrument (ϕ) does not enter into the calibration factor C_λ according to (14).

In practice, first the angle ϕ is measured relative to gravity by means of a bubble inclinometer. Using a laser level, the height of the lamp is set to be equal to the centre of the screen. Then, α is simply equal to 90°–ϕ. The distance from the screen to the lamp is then measured using a laser distance meter.

Given that with this setup there are only two critical measurements, the screen angle α and the distance z from the screen to the lamp, an elementary uncertainty analysis can be performed. Ignoring constants, and dropping the subscript λ because it applies to instruments that acquire data as a function of wavelength, the geometrical form of (18) is:

$$C \sim \frac{\cos\alpha}{z^2}. \tag{19}$$

The absolute uncertainty, δC, is determined by:

$$\delta C^2 = \left|\frac{\partial C}{\partial z}\right|^2 \delta z^2 + \left|\frac{\partial C}{\partial \alpha}\right|^2 \delta\alpha^2 \tag{20}$$

$$\delta C = \sqrt{\frac{4\cos^2\alpha}{z^6}\delta z^2 + \frac{\sin^2\alpha}{z^4}\delta\alpha^2}. \tag{21}$$

The relative uncertainty can be found by dividing (21) by C:

$$\frac{\delta C}{C} = \sqrt{\frac{4}{z^2}\delta z^2 + \tan^2\alpha\delta\alpha^2}. \tag{22}$$

To illustrate the impact of the two parameters and their uncertainties on the relative uncertainty in (22), Figure 4 shows the percent relative uncertainty as functions of δz and $\delta\alpha$. In the case of a small value of α such as 15 degrees, the contribution to $\delta C/C$ from $\delta\alpha$ in degrees is comparable to that of δz in dm. Yet for larger α, the contribution to $\delta C/C$ is clearly dominated by $\delta\alpha$. Thus, the relative uncertainty in the calibration factor, C, is minimized by keeping z and α respectively as large and small as possible.

Practical constraints to z and α are important to note. With a common bubble inclinometer, it is doubtful to be able to measure α to better than 2-3 degrees. Also, since the location of each instrument in the observatory is fixed, so are values of z for the different instruments. In addition, while (22) and Figure 4 indicate that α should be minimized, the projected area of α towards the instrument is proportional to sin α. Thus, there is a limit to how small α can be without violating the assumption that the screen totally fills the instrument's field of view.

Finally, if there is a height difference between the lamp and the screen, α is no longer equal to 90°–ϕ. In this case, (19) becomes

$$C \sim \frac{1}{z^2}\cos\left[90^\circ - \phi + \tan^{-1}\left((h_{lamp} - h_{screen})/z\right)\right], \tag{23}$$

and the uncertainty analysis can be redone. However, with z being so much larger than any reasonable height difference between the screen and the lamp, the effect on the relative uncertainty is minor. For example, the height difference required to produce a 1 degree change in α is 87 cm when z = 50 m. But if a differential height error does occur, it is helpful to have the screen be above the lamp, thus reducing α and the overall relative uncertainty.

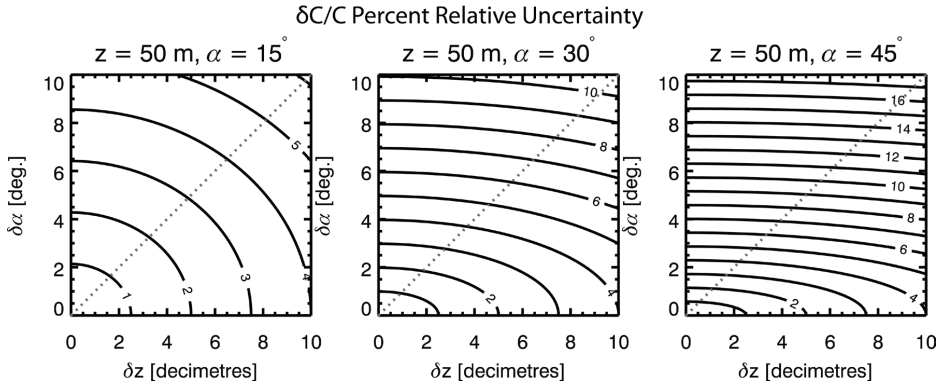

Figure 4. Variation of relative percent uncertainty in Equation 22 with distance δz and screen angle $\delta\alpha$. The dotted grey line indicates a slope of unity. The largest practical screen-lamp distance z = 50 m for field calibrations at KHO was chosen to illustrate the effect of screen angles 15, 30 and 45 degrees.

1.1.4. Calibration of digital single lens reflex cameras and their applications in aeronomy

Recent technological advances in consumer electronics have made Digital Single Lens Reflex (DSLR) cameras emerge as an inexpensive option for applications in aeronomic research. The ability to easily change many parameters on the camera, such as the lens, apertures, exposure time, etc., permits a flexibility not commonly found in expensive, custom-built optical systems that typically have a narrow set of scientific applications. This section describes how each of the colour channels of the DSLR can be calibrated absolutely in a laboratory. Some example applications of DSLR data will be given.

Modern DSLR cameras typically use either a CCD or a Complementary Metal Oxide Semiconductor (CMOS) sensor. On top of the detector is a composite array of filters and microlenses called a Colour Filter Mosaic (CFM). It is required to detect photons of different wavelengths corresponding to either primary or secondary colours used in forming a colour image. The most common CFM is known as a Bayer mosaic, which has two green, one red and one blue pixel, in order to account for the green bias of the human eye. This is shown schematically in Figure 5. An example alternative mosaic that uses secondary colours is a Cyan, Yellow, Green and Magenta (CYGM) array. A raw image on the detector is converted to a colour image by a demosaicing algorithm, specific for each CFM.

Calibration measurements of the individual colour channels of the Nikon D70 and D200 were performed in Paper II. The Nikon D80 was calibrated in a similar fashion in *Peters* [2009]. In contrast to the preceding calibration section, where the instrumental response as a function of wavelength (i.e. the instrument function) was known, a different technique is needed in order to quantify the relatively wide passbands of each of the colour filters in the CFM. Specifically, the light source is changed from a broadband tungsten lamp to a more narrowband source, as described below.

The method used to calibrate DSLRs in the UNIS calibration lab consists of the camera

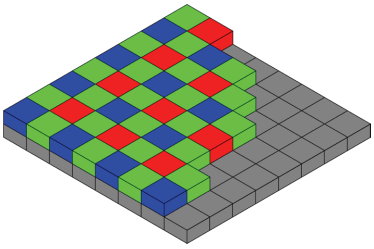

Figure 5. Diagram of Bayer colour filter mosaic [*Burnett*, 2006].

viewing a Lambertian screen or integrating sphere, illuminated by output from a monochromator. The HR320 Czerny-Turner monochromator produces narrow lines of approximately 1.2 nm bandwidth, varying from 400–700 nm. Both the camera and a calibrated CCD spectrograph observe the exitance from the screen (or sphere) over the 31 lines output from the monochromator over the visible range, as shown in Figure 6.

These data can be used to produce a measurement of the spectral responsivity for each colour channel of a DSLR. For a unique observation *i* of the source, the number of raw counts (cts) for a given pixel is expressed by:

$$u_i^{(k)} = \int C_i(\lambda) \cdot S^{(k)}(\lambda)\, d\lambda\,, \quad [cts] \tag{24}$$

with $C_i(\lambda)$ being the absolute intensity of the source [*R*] and $S^{(k)}(\lambda)$ the spectral responsivity in *cts* R^{-1} [*Chang and Chen*, 2001]. In the above configuration, $C_i(\lambda)$ is determined using the output from the CCD spectrograph acquired at the time of the DSLR image for a given setting of the monochromator. Since the monochromator produces 31 lines, (24) can be expressed as a matrix equation, representing an observation set:

$$\hat{u}^{(k)} = C \cdot \hat{S}^{(k)},\ C = \left[C_1 C_2 C_3 \cdots C_{31}\right]^T \tag{25}$$

yielding the spectral responsivity over the entire wavelength range by solving for $\hat{S}^{(k)}$. This calibration method and the above equation both assume that the spectral responsivity is independent of wavelength over the monochromator bandwidth of ~1.2 nm.

One practical matter to note is that the background should be subtracted from each pixel before (25) is computed. This is done by taking an image with identical settings as

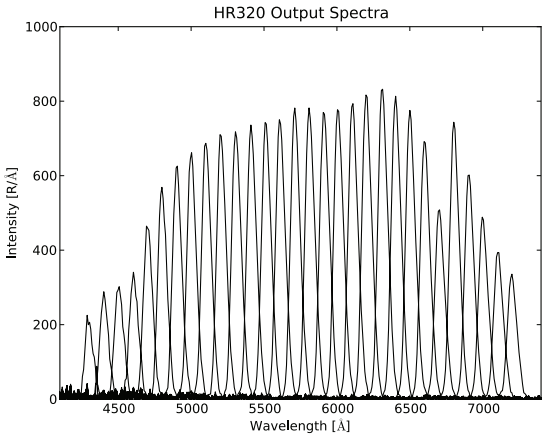

Figure 6. Absolute intensity of source 31 lines output from the integrating sphere-illuminated HR320 monochromator, as measured by the FICS CCD spectrograph. The line shape is a convolution of various optical components from lamp to detector, as discussed in Paper II.

when viewing the source, except in total darkness. This acts to account for any stray or background light in the calibration room. The detector bias should also be removed from the images before the calibration procedure. In practice, subtracting the counts recorded by the camera with the smallest possible exposure time (e.g., 1/8000 sec. for the D200) removes the bias. Considering that the nominal exposure times of the three DSLRs considered tend to be 4 seconds or greater for auroral imaging, the detector bias has a negligible effect.

Spectral responsivities for the Nikon D70 and D200 (left) and the D80 (right) are shown in Figure 7. Superposed on both panels are typical dayside and nightside spectra obtained by the meridian-imaging auroral spectrograph (ASG) of the Japanese National Institute for Polar Research (NIPR) and Tohoku University. Note that the method is the same, but the depiction is different for the left and right panels. Figure 7a shows the spectral responsivity in units of 10^6 *cts* R^{-1}, while in Figure 7b the responsivity has been divided by the exposure time, resulting in units of *cts* R^{-1} s^{-1}.

From the ASG spectral profiles shown in the figure below, it is clear that prominent auroral emissions such as λ427.8, λ557.7 and λ630.0 nm are shifted relative to the passband peaks of the blue, green and red channels of these cameras, respectively. But the colour response of the DSLR sensor was not designed with atmospheric research in mind; it is chosen to emulate the human eye response. Nevertheless, assuming the mean auroral energy to be relatively low, one can expect the emissions measured in each of the channels of the DSLR to be from the three common wavelengths indicated above. On the other hand, in situations where multiple auroral emissions are present within each colour passband (e.g., high energy nightside aurora with molecular band structures), the DSLR is

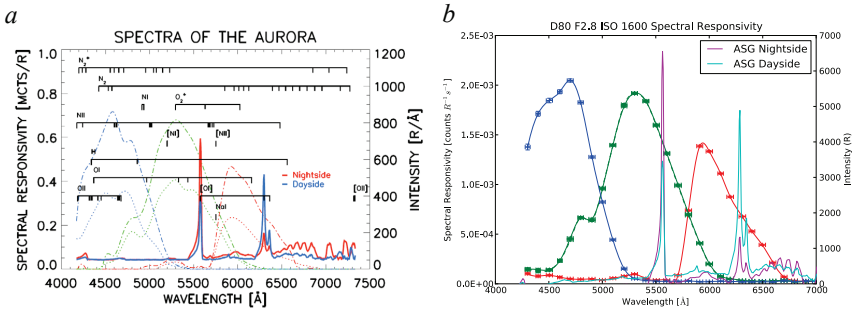

Figure 7. Spectral responsivities of different Nikon DSLRs obtained in two different studies. Left: red, green and blue channel responsivities for the D70 (dotted lines) and the D200 (dot-dashed lines) from Paper II. Common auroral emissions are shown by black tick marks, with typical dayside (solid blue) and nightside (solid red) spectra. Right: spectral responsivity of D80, with error estimates for red, green and blue channels (after *Peters* [2009]). Responsivities are valid for 4 sec. exposure time and ISO 1600 on all three cameras.

not able to discriminate between them. But despite such events, the emissions listed above are still the dominant emission lines above Svalbard. Finally, the presence of non-auroral, broadband light such as twilight can saturate one or more colour channels with a too long exposure.

DSLR imagery is useful in any application where a multicolour image adds additional information. An example is the use of colour to distinguish between cloud cover and a slowly moving auroral feature. This is in contrast to traditional auroral imaging, which nearly always images over a very narrow wavelength interval (~ nm) at any particular time. Of course, a modern all-sky imager using a filter wheel can take three narrowband images at λ427.8 nm, λ557.7 nm and λ630.0 nm in a sequence, but the images are taken at different times. Furthermore, it is sometimes necessary to eliminate or change one or more filters from the imaging sequence, depending on the scientific application.

While the data from the DSLR in operation at KHO have not been fully exploited, they have initially been applied to detecting cloud cover and determining the general sky conditions when other, more sensitive instruments cannot be operated (e.g., during moonlit or intense twilight periods). Figure 8 shows two images from the DSLR operated at KHO by NIPR, both under clear sky conditions. The dayside image, Fig. 8a, shows twilight in the south (top), cloud cover illuminated by Longyearbyen city lights (bottom, left of centre), and auroral red and green structures typical of dayside aurora. Fig. 8b depicts

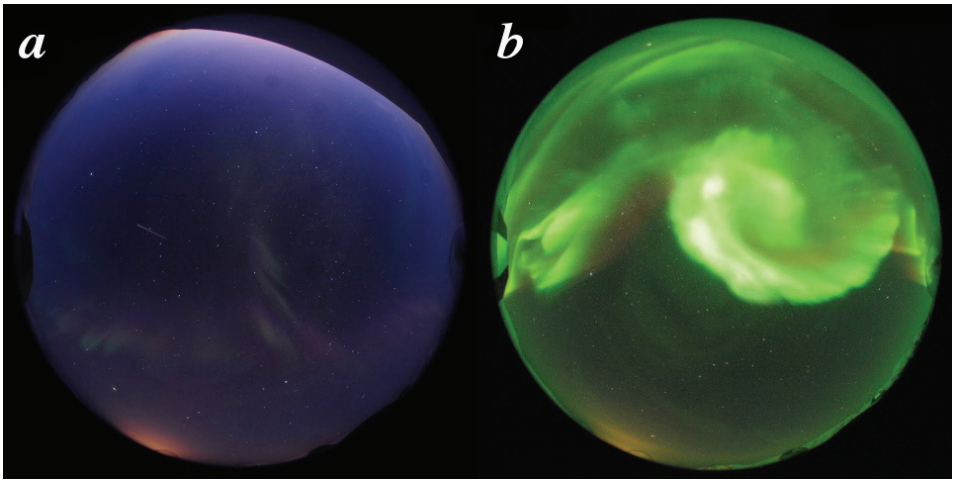

Figure 8. Two DSLR images from KHO, representative of typical auroral conditions on Svalbard. Equipment used is a Nikon D700 and an 8 mm Nikkor F/2.8 circular fisheye lens, with an exposure time of 8 sec. at 6400 ISO. Dayside aurora acquired on 2010 Jan. 11 at 08:10:20 UT (a). Aurora, as part of a substorm poleward expansion, acquired on 2010 Nov. 10 at 18:45:40 UT (b). South is at the top; East on the right. Images courtesy of H. Miyaoka, NIPR.

substorm aurora above the observatory. In this picture, red aurora is seen above (i.e. closer to the image centre) brighter green emissions during the substorm poleward expansion.

There are some drawbacks to using DSLRs. The recent industrial momentum to produce cameras with progressively higher resolution (i.e. total pixel count), without appreciable increase in sensitivity, does not well serve their application to low light imaging. Even the smallest picture setting possible on the Nikon D80 produces 1936× 1296 pixel images (2.51 megapixels) – hardly necessary for anything other than public relations purposes without a proportional increase in sensitivity. When using a scientific CCD for low light imaging, the image size is usually set such that a balance is achieved between sensitivity and needed spatial resolution. For example, some modern scientific CCD systems in aeronomic research use image sizes as small as 256×256 pixels, or 0.06 megapixels.

In addition, the shutter and mirror mechanisms in a DSLR will eventually wear out, which has happened already with one camera at KHO. There exist colour detectors with longer-lasting electronic shutters that are designed to cater to both the amateur astronomy and Closed Circuit Television (CCTV) communities. These are an attractive, workable alternative, but they are somewhat of a step to a higher price range than commonly available DSLRs. An example colour system, and further discussions of the application of colour imaging in auroral research can be found by *Partamies et al*. [2007].

Despite possessing moving parts and having lower sensitivity than research-grade imaging systems, commercially available DSLR systems are increasingly finding their place in aeronomic / auroral research as inexpensive context instruments. In addition, their low cost permits their deployment in multiple locations where multiple look angles are required, for example in auroral triangulation or sounding rocket experiments.

1.2. Proton aurora

The aurora is a phenomenon caused by the precipitation of energetic particles whose interaction with the upper atmosphere can produce fascinating displays of light. While whimsical and certainly impressive, the study of the particle characteristics and the light they produce provides real insight into the interactions between the solar wind, the magnetosphere, and finally the Earth's neutral and ionized upper atmospheric regions: the thermosphere and ionosphere, respectively.

The majority of particles comprising the solar wind, the same particles that precipitate into the upper atmosphere, are electrons and protons. Through various interaction

processes, particle precipitation energizes atmospheric constituents and produces ionization. In excited states, atmospheric atoms and molecules emit photons with energy less than or equal to that which is imparted to them, thereby producing aurorae.

Photons emitted in atmospheric reactions involving precipitating electrons, termed electron aurorae, are the most commonly studied optical diagnostic used to understand magnetosphere-ionosphere coupling; magnetospheric topology, particle distributions and current systems; ionospheric and thermospheric composition and dynamics, and so on. While many fine details of the nature of these phenomena will occupy researchers for decades, possibly centuries to come, electron aurorae are generally better understood than those created by precipitating protons.

1.2.1. Hydrogen spectra and thermospheric proton precipitation

1.2.1.1. Discovery and phenomenology

Precipitating protons of magnetospheric origin are initially confined to a magnetic flux tube. Upon interaction with upper atmospheric particles, part of the proton population will undergo charge exchange reactions, capturing an electron to form neutral hydrogen of comparable kinetic energy. Subsequent charge stripping and capture reactions result in a heterogeneous proton/hydrogen (H^+/H) population, as schematically illustrated by Figure 9. Since some of the incident particles are electrically neutral hydrogen, they are not subject to the Lorentz force that produces the charged particles' helical trajectories. A neutral hydrogen atom moves freely across magnetic field lines and retains a pitch angle similar to the incident proton. A H^+/H beam at the top of the thermosphere will therefore become more transversely extended with decreasing altitude. In addition, the proton gyroradius itself is typically hundreds of meters (~200m at 5 keV). Thus, emitted photons from the hydrogen component of the population, known as proton aurorae, exhibit a more diffuse character relative to discrete electron aurorae that do not suffer such effects [*Vallance Jones*, 1974]. These hydrogen emissions are the unique signature of proton aurorae, as precipitating electrons do not generate them to any detectable threshold.

Lars Vegard was the first to detect a Doppler shift in auroral hydrogen Balmer emissions (H_α λ656.3 and H_β λ486.1 nm) from the ground with spectral measurements beginning in 1921 [*Vegard*, 1939]. This discovery not only provided evidence of proton precipitation in the auroral regions, but also significantly supported the theory that auroral emissions, in general, are caused by precipitating particles [*Vegard*, 1948]. The finding of the Doppler–shifted and –broadened line profiles was confirmed decades later by *Gartlein*

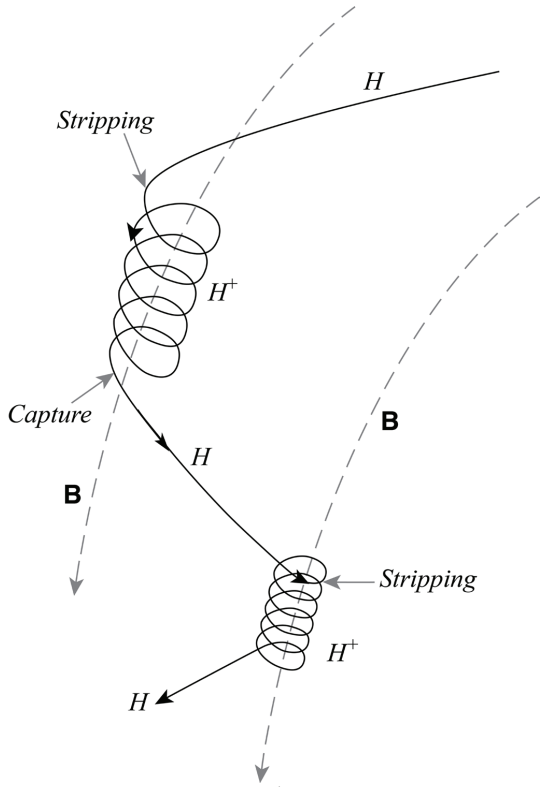

Figure 9. Schematic depiction of a precipitating H^+/H particle trajectory. From top: incoming H particle undergoes charge stripping ($H + M \rightarrow H^+ + M + e^-$), is confined to helical trajectory about **B**, captures an electron ($H^+ + M \rightarrow H^{(*)} + M^+$), and so on. After *Davidson* [1965] and *Simon* [2006].

[1950], and with higher spectral resolution measurements by *Meinel* [1951].

Measurements of the Balmer Doppler profile at multiple look angles showed shifts and broadening that varied between the magnetic zenith and horizon directions. Observations toward the magnetic horizon produced profiles that were symmetric about the unshifted line, or rest wavelength. By contrast, magnetic zenith profiles showed a clear asymmetry. The profile peak was blue-shifted ~0.5 – 0.7 nm, and was more broadened toward shorter wavelengths [*Eather and Jacka*, 1966]. Since only particle motions along the observed line-of-sight contribute to the Doppler effect, only the particles' gyroscopic motion and their distribution in pitch angle produced the symmetric broadening in the magnetic horizon profiles. The distribution of particle velocities parallel to the magnetic field produced both Doppler broadening and peak shift when observing in the magnetic zenith. Early theoretical formulations were able to describe the general behaviour of proton precipitation and hydrogen emissions, including accounting for this variation with observation direction [*Chamberlain*, 1954a, 1954b, 1957; *Omholt*, 1956; Tuan, 1962].

Eather [1967] reviewed the state of proton auroral research at the conclusion of the 1960s. More recent reviews include *McNeal and Bierly* [1973], *Eather* [1988], *Rees* [1989], *Yevlashin* [2000], *Basu et al*. [2001] and *Galand and Chakrabarti* [2006].

The blue-shifted wing of the Doppler profile was found to vary with magnetic local time (MLT), with narrower spectra and smaller mean Doppler shifts found on the dayside than the nightside. Its interpretation as proportional to the line of sight-integrated H^+/H energy spectrum supports the notion that lower energy proton precipitation can be found near the dayside cusp [e.g., *Derblom*, 1975; *Henriksen et al*., 1985], and higher energy proton precipitation is found in the evening and on the nightside [e.g., *Galand et al*., 2004; *Borovkov et al*., 2005]. Figure 10 illustrates the variation of the Doppler profile in H_α between the night- and dayside. This general pattern of proton precipitation is also confirmed by satellite particle measurements [*Hardy et al*., 1985].

Interestingly, a smaller, but significant component in the magnetic zenith profiles indicated upward-moving H^+/H particles in the form of a red-shifted wing. While initially believed to be due to magnetic mirroring of protons [*Eather and Burrows*, 1966], the relatively coarse instrumental spectral resolution made it difficult to unambiguously attribute the red shift to upward moving particles [*Eather*, 1966]. This is because the instrument functions of previous decades ($\geq$ 1.0 nm) convolved with even unshifted hydrogen Doppler profiles resulted in a component of the profile at longer wavelengths. However, higher spectral resolution instruments ($\leq$ 0.5 nm) deployed after 1980 have unambiguously detected red shifts attributed to upward moving H^+/H particles [*Lummerzheim and Galand*, 2001; *Lanchester et al*., 2003]. Specific attention to this 'albedo flux' is given in the context of its contribution to the population of Energetic Neutral Atoms (ENA) of terrestrial origin, found in near Earth space [Søraas and Aarsnes, 1996; Synnes et al., 1998].

1.2.1.2. Recent theoretical and observational advances

In the 1960s, researchers built upon initial theoretical attempts of the previous decades in order to more quantitatively and accurately describe proton precipitation. From this time, the modelling efforts fall into three disparate categories: The Continuous Slowing Down Approximation (CDSA), Monte Carlo (MC) methods, and Linear Transport (LT) theory [*Decker et al*., 1996]. The CDSA is based on semi-empirical range-energy relations for H^+/H particles in air, derived from laboratory results. This formulation uses the notions of stopping power and particle range, which are mature concepts from laboratory research. An expression for the energy loss of a H^+/H particle, ΔE , between from an initial height h_0

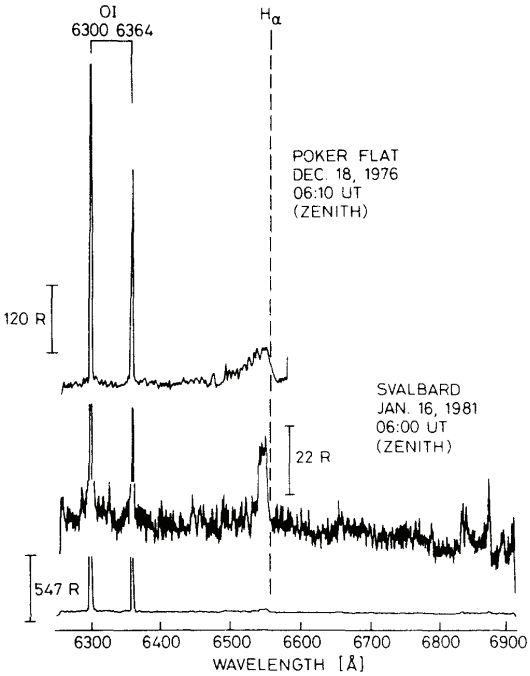

Figure 10. Depiction of H_α Doppler profile variation. Broad nightside spectrum obtained at Poker Flat, Alaska (top), and narrower dayside spectrum from Svalbard (bottom). Sites are separated in MLT by approximately 10 hours. Spectra were obtained with the same spectrograph. After *Henriksen et al.* [1985].

down to an arbitrary height h_1, in steps of δh, is given by:

$$\Delta E(h,\alpha) = \frac{1}{\cos\alpha} \sum_{h'=h_0}^{h_1} \frac{dE}{dR(E)} \frac{n(h')}{n_0} \delta h \,, \tag{26}$$

with n, α, and R being the atmospheric density, pitch angle relative to the magnetic field, and range, respectively [*Henriksen*, 1979]. Here, the energy degradation coefficient *dE/dR(E)* is analogous to stopping power.

Edgar et al. [1973, 1975] were the first to implement the CDSA for proton aurora. It was also applied specifically to the transverse spreading of H^+/H particles by *Johnstone* [1972] and *Iglesias and Vondrak* [1974]. *Henriksen* [1979] determined that the atmosphere attenuates precipitating H^+/H particles in approximate proportion to their pitch angle. Modern implementations of this technique, applied to simulating both the Balmer volume emission rates and ground-based Doppler profiles, are found and discussed by *Sigernes et al.* [1994] and *Sigernes* [1996, and references therein].

The next method, called the Monte Carlo technique, tracks individual precipitating H^+/H particles and their interactions with the atmosphere as governed by probabilistic expectations. The particle trajectories are governed by two factors, the first being that precipitating protons in a converging magnetic field experience changes in pitch angle according to the adiabatic invariance of the magnetic moment [e.g., *Parks*, 2003]:

$$\mu = \frac{mv^2 \sin^2 \alpha}{2B} = const. \tag{27}$$

It therefore follows that a precipitating proton encountering a stronger magnetic field magnitude increases its pitch angle. Second, the neutral hydrogen atom travels in a straight line, despite the presence of the converging magnetic field. The change in pitch angle of a hydrogen atom in a dipolar magnetic field from heights h_0 to h_1 is found through geometry:

$$\Delta\alpha = \tan^{-1}\left|\left(1 - \frac{h_0 + R_E}{h_1 + R_E}\right)\tan\alpha\right|, \tag{28}$$

where R_E is the Earth's radius [*Kozelov*, 1993].

The essence of this technique is that the free path length τ of an H^+/H particle between interactions is randomly determined by:

$$\xi = \exp(-\tau); \quad \tau = \int_{h_0}^{h_1} \frac{dh'}{\cos\alpha(h')} \sum_{i,j} n_i(h') \sigma_{i,j}^{tot}(E_0), \tag{29}$$

where ξ is a uniformly generated random number between zero and one, E_0 is the energy of the particle after the interaction at h_0, and the $\sigma_{i,j}^{tot}$ are the cross sections for the interaction between the neutral specie i with the particle with charge state j. In addition to elastic scattering, the possible interactions are:

Charge capture	$H^+ + M \rightarrow H^{(*)} + M^+$
Charge stripping	$H + M \rightarrow H^+ + M + e^-$
Ionization	$H^+ + M \rightarrow H^+ + M^+ + e^-$
	$H + M \rightarrow H + M^+ + e^-$
Excitation	$H^+ + M \rightarrow H^+ + M^*$
	$H + M \rightarrow H + M^*$
	$H + M \rightarrow H^* + M$

First implemented by *Davidson* [1965], the MC simulations showed a substantial broadening of a H^+/H beam with decreasing altitude. This corroborated then contemporary

ground-based optical measurements of diffuse Balmer emissions spread over a wide region [e.g., *Eather*, 1969]. Subsequent applications of the method were made by *Ponomarev* [1976], *Galperin et al*. [1976] and *Kozelov and Ivanov* [1992]. The first MC simulation using a dipolar magnetic field and a three species atmosphere was performed by *Kozelov* [1993]. *Lorentzen* [2000] used a similar setup to describe the H^+/H beam spreading effect in latitude and longitude. Further characterization of beam spreading and its effect on ionization and conductances in the ionosphere and neutral atmosphere were conducted by *Fang et al*. [2007, and references therein].

In recent years, simulations of H^+/H transport using MC formalism have been compared to ground- and space-based data with increasing success. *Kozelov* [1996] validated model output with *in situ* rocket-borne particle measurements of *Søraas et al*. [1974]. *Lorentzen et al*. [1998] used satellite particle data as input to an MC simulation; the simulated Doppler profiles matched well with ground-based spectrometer measurements. A comparison of simulated H_α profiles with modern CCD spectrograph data during substorm onset is illustrated by *Borovkov et al*. [2005]. In that study, observations showed two distinct populations of H^+/H particles (~30 and ~60 keV), co-located with N-S electron arcs.

Collisional angular redistribution has been included in the MC model of *Kozelov and Ivanov* [1992], and later *Gérard et al*. [2000], to more accurately reproduce the red-shifted (or blue-shifted for space-based observations) wing of the Doppler profile. The model output was used to compare both observations of Lyman α from space [*Gérard et al*., 2001] and Balmer β from the ground [*Gérard et al*., 2005].

From this analysis, the authors indicate how the full line shape of the Doppler profile must be used to infer estimates of the H^+/H energy distribution, as opposed to only using the Doppler shift of the peak intensity. This is because different physical processes involved in H^+/H precipitation contribute differently to the shape of the profile. For example, the presence of higher energy H^+/H particles produces photons of higher blue shift, extending the blue-shifted wing of the Doppler profile and shifting the peak to shorter wavelengths. On the other hand, the same particles undergo more collisions than lower energy particles, and are thus more isotropized. This leads to an enhancement in the Doppler profile at the rest wavelength, thus weighting the profile peak back towards the rest wavelength [*Gérard et al*., 2005].

Linear transport theory explicitly solves the coupled H^+/H Boltzmann equations along the magnetic field line either analytically or numerically, and is nominally a one-

dimensional framework. Initially applied by *Jasperse and Basu* [1982], their model used a uniform magnetic field, a plane-parallel geometry, and steady state conditions. A spreading factor was introduced to account for the broadening of the H^+/H beam with decreasing altitude. While the model ignored the ionization produced by secondary electrons, a modified model self-consistently solved for the combined hydrogen, proton and electron fluxes [*Basu et al*., 1993; *Strickland et al*., 1993]. One interesting result from the latter study was that the secondary electron flux resulting from H^+/H precipitation was found to be softer, or less energetic, than for that of primary electron precipitation. *Jasperse* [1997] adapted the model using matched asymptotic expansions to revisit the effect of H^+/H beam spreading.

Galand et al. [1997, 1998] significantly advanced the modelling effort when they developed a LT model that solved the dissipative, coupled H^+/H Boltzmann equations. One strength of the technique is that since the solution to proton energy degradation is analytic, the model can be run quickly and with a minimum of computational resources. In addition, this model made major headway regarding the inclusion of both magnetic mirroring and collisional angular redistribution of H^+/H beams. It was found that while both processes contribute to the overall albedo flux of H^+/H particles, magnetic mirroring acts to reflect particles primarily above the optical emission region of typically 100 – 300 km, thereby not contributing significantly to the detected Doppler-shifted red wing [*Galand et al*., 1998, 1999].

In addition, with *in situ* particle data from satellites as input, this model produced Doppler profiles that matched well with high resolution, ground-based spectra. Thus, provided such realistic modelling, the hydrogen Doppler profile can be used to estimate energy flux and characteristic energy of precipitating H^+/H particle populations [*Lanchester et al*., 2003]. This is quite advantageous, considering satellite overpass timing and geometry are rarely ideal.

Simon [2006] developed a kinetic/fluid transport electron-proton transport code. Based on a synthesis of the kinetic proton model of *Galand et al*. [1997, 1998] and the TRANSCAR electron transport code [*Lilensten and Blelly*, 2002], it is unique in that for a given influx of protons, it simultaneously and self-consistently computes both the proton and electron kinetic transport and the associated fluid equations, including convection effects and collisional and magnetic angular redistribution. Model output agreed well with ground-based H_α spectra, and also radar-derived electron density resulting from simultaneous proton and electron precipitation. In the latter case, the model indicates the

relative contribution of proton and electron precipitation to the total electron density profile as seen by the EISCAT Svalbard Radar [*Simon et al*., 2007].

Kozelov and Holmes [2008] presented new arguments regarding the simulation of the Doppler profile in hydrogen aurora. They used a new version of the Kozelov MC model with a collision-by-collision algorithm that accounts for scattering reactions specific for the different atomic states of hydrogen. For the occurrence of the red-shifted wing of the profile, they conclude that it is not necessary to assume a large average scattering angle for all charge exchange reactions, as was done in other modelling which contradicts currently available cross section data. Instead, angle scattering reactions consistent with available cross sections are shown to reproduce a substantial red-shifted wing when accounting for individual reactions for each final atomic state. Specifically, only excited hydrogen atoms are found to scatter to large angles, and thus contribute to the red-shifted wing of the Doppler profile.

1.2.2. Dayside proton aurora as a visible tracer of magnetopause boundary layer dynamics

The polar cusps are high latitude regions found in the dayside magnetosphere where solar wind particles have unmitigated access to the Earth's lower magnetosphere and ionosphere. They appear as funnel-like structures where the Earth's magnetic field

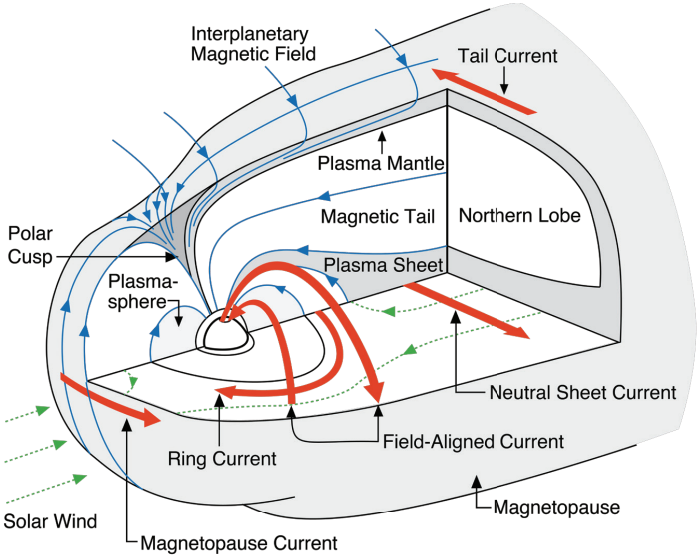

Figure 11. Cutaway view of the Earth's magnetosphere. Magnetic field lines are depicted in blue, plasma flows in green, and currents in red. Only the northern hemisphere cusp is shown. After *Russell* [2000].

weakens and bifurcates [e.g., *Tsyganenko and Russell*, 1999]. Figure 11 shows a projection of the magnetosphere and its different regions. For typical conditions, the terminus of the cusps in the upper atmosphere is located approximately near ±75° magnetic latitude (MLAT), has ~1° latitudinal width, and is 5–6 hours wide in magnetic local time [*Johnsen and Lorentzen*, 2012]. Ground-based observatories with the best combination of appreciable winter darkness and proximity to the cusp are shown in green in Figure 12.

Recent decades of dayside auroral research have emphasized the study of the cusps and neighbouring magnetospheric boundary layers in order to learn more about the coupled solar wind-magnetosphere-ionosphere system (see review by *Frey* [2007], and references therein). When the merging of the solar wind magnetic field with that of the dayside magnetosphere occurs, constrained magnetosheath and magnetospheric particles can precipitate to create dayside and cusp aurorae, which often occur directly above Svalbard. Researchers have been using these auroral signatures as tracers of processes such as magnetic merging occurring at the low latitude (sometimes described specifically as sub-solar) magnetopause, and lobe merging, occurring at higher latitudes.

During dayside magnetopause merging, the interplanetary magnetic field (IMF) connects with magnetospheric field lines, leaving the resulting flux tubes opened to the

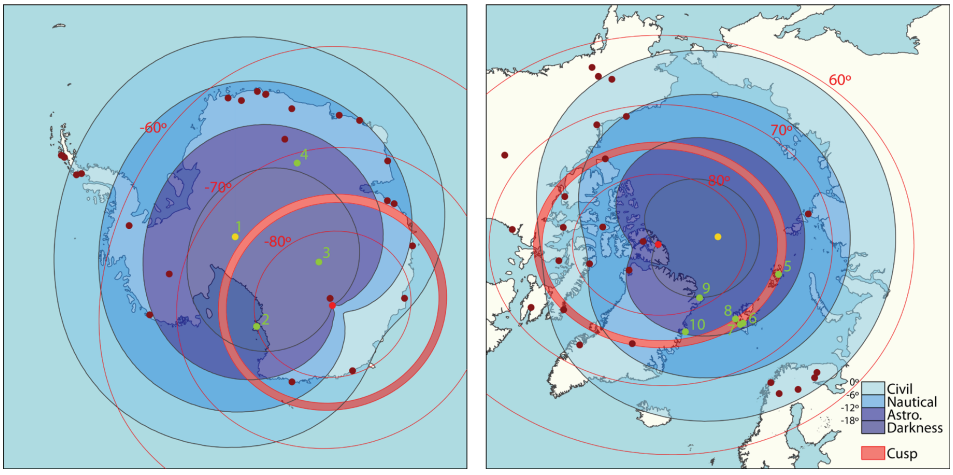

Figure 12. Magnetic noon values of solar elevation angle (SEL, black lines) and twilight (blue shading) during the winter solstice, for the Antarctic (left) and arctic (right) regions. AACGM magnetic latitudes (epoch 2010) are overlaid as red lines. Magnetic poles are red dots; geographic poles are gold dots. A 1° 'typical' optical cusp (valid for IMF $B_z \sim 0$), from 75.4°-76.4° MLAT is shown as a red band [*Johnsen and Lorentzen*, 2012]. Observatories well located for optical cusp measurements (SEL lower than -12° and within viewing distance of cusp auroral altitudes above 10° elevation angle) are indicated as numbered green dots. Suitable stations include: 1. South Pole, 2. McMurdo, 3. Vostok, 4. Dome Fuji, 5. Heiss Island 6. Longyearbyen, 7. Barentsburg, 8. Ny-Ålesund, 9. Station Nord, 10. Danmarkshavn. For comparison, other existing and historical stations are shown in dark red.

IMF on one end and connected to the geomagnetic field on the other. This newly opened flux is swept antisunward owing to prevailing magnetospheric convection [*Dungey*, 1961]. Intermixed magnetosheath and magnetospheric ion populations confined to the convecting flux tubes are accelerated; those with the highest velocity parallel to the magnetic field precipitate into the ionosphere first. This is shown schematically in Figure 13. Since at least two disparate ion populations are subject to this process, it is not surprising that a dispersion of precipitating ion energy with space and time occurs as the flux tube convects tailward. This is known as the ion velocity filter effect, first observed by satellites at high latitudes and altitudes in the plasma mantle [*Rosenbauer et al.*, 1975; *Haerendel*, 1975]. The effect also manifests in the form of ion distributions with low energy cut-offs that have been used to investigate the location and plasma properties of the magnetopause reconnection site [*Onsager and Elphic*, 1996, and references therein]. Low altitude, polar-orbiting satellite measurements of this energy dispersion were also reported in and near the cusp, showing pulsed, stepped, and smooth ion dispersions along the spacecraft trajectory [*Newell and Meng*, 1988]. But because of the spatio-temporal ambiguity inherent in these measurements, the energy dispersions were difficult to interpret relative to magnetopause reconnection events [*Lockwood and Smith*, 1989].

Meanwhile, combined satellite and ground-based observations related the dayside

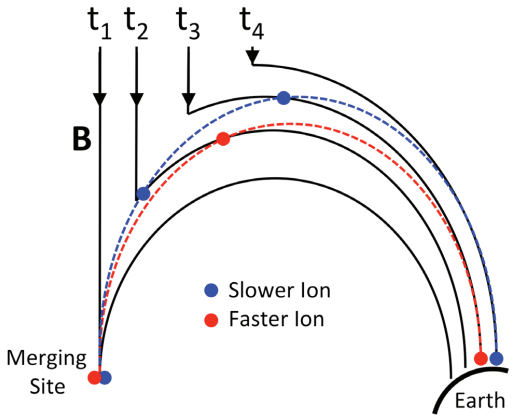

Figure 13. Depiction of the ion velocity filter effect for newly merged magnetic field lines (black). At time t_1, the arbitrary high (red) and low (blue) parallel energy particles are collocated after the initial merging. During $t_1 < t < t_3$, field-aligned acceleration and velocity dispersion occurs. At time t_3, the faster particle precipitates into the ionosphere, followed by the slower particle at higher MLAT at time t_4. After *Onsager and Elphic* [1996].

electron auroral features to flux transfer events (FTEs) at the magnetopause [*Russell and Elphic*, 1978, 1979], and illuminated the relationship between auroral dynamics and transient magnetopause merging [*Sandholt et al.*, 1986]. Polar Moving Auroral Forms (PMAFs), attributed primarily to precipitating electrons, were discovered to be good candidate signatures of such ionospheric responses [*Fasel*, 1995]. Previously published characteristics of PMAFs consistent with FTEs and transient magnetopause merging are discussed by *Sandholt et al.* [2002, and references therein].

Spectra of H^+/H emissions were observed from the ground with improved time resolution, revealing the pulsed nature of dayside proton precipitation on time scales similar to PMAF occurrence [*Sigernes et al.*, 1996]. These hydrogen emissions were sometimes observed with an accompaniment of discrete electron auroral arcs, both on the dayside, often as PMAFs [e.g., *Lorentzen et al.*, 1996, *Lorentzen and Moen*, 2000], and in nightside substorm aurora [e.g., *Deehr*, 1994, *Deehr and Lummerzheim*, 2001]. Despite the spatio-temporal coincidence of FTEs during dayside merging and PMAFs, no single theory linking the two phenomena has emerged. On the contrary, observations of dayside H^+/H precipitation and supporting theory consistently illustrate the relationship with dayside magnetic merging [*Deehr*, 2002].

Spectral measurements of the hydrogen Doppler profile showing sudden changes in energy combined with the Pulsed Proton Events (PPEs), observed during magnetopause merging [*Sigernes et al.*, 1996], motivated new hypotheses [*Deehr et al.*, 1998]. The first was that latitudinally distributed, ground-based optical measurements of precipitating H^+/H energy should reveal the ion velocity filter effect as well. Also, the variation of H^+/H energy with time above the observatories could be used as a proxy for the merging rate at the magnetopause.

The Protonics project was initiated to further explore these concepts. Using spectral measurements of Balmer α and β from both Longyearbyen and Ny-Ålesund, the ion velocity filter effect was observed for three different cases, described in Papers III and IV. The first ground-based observations of the velocity filter effect in Paper III required the energy difference between the stations to be averaged for up to two hours in order to be statistically significant. The last case in Paper IV features Doppler profiles of sufficiently high signal-to-noise ratio that the energy difference between the two stations could be observed in a time-resolved, scan-by-scan fashion. Not only was a 2-5 keV energy difference observed over a period of 45 minutes, but also the difference increased throughout the period, indicative of a decreasing merging rate at the magnetopause.

1.3. Proton and electron shock aurora

The solar wind is replete with different discontinuities and shocks that affect the magnetosphere-ionosphere system. Those associated with sudden enhancements in the solar wind ram (or dynamic) pressure, P_{ram}, produce a compression of the dayside magnetosphere; the general term "pressure pulse" describes this enhancement. In turn, the compression intensifies the Chapman-Ferraro currents (also known as the magnetopause currents, cf. Figure 11), moving them nearer to Earth. The response of the horizontal component of the magnetic field at the Earth's surface to this enhancement is termed a geomagnetic Sudden Impulse (SI). They are observed typically within one minute of the shock impingement on the magnetopause, dictated approximately by the Alfvén speed. When such an impulse is followed by a geomagnetic storm, the term Storm Sudden Commencement (SSC) is used, although morphologically SI and SSC are identical [*Nishida*, 1978].

Some effects of sudden increase in P_{ram} associated with shocks and/or pressure pulses include, for example, the energization of trapped particle populations, creation of new radiation belts, and propagating auroral brightenings termed shock aurorae. In addition, in situations where a significant, concurrent IMF turning is observed, a net input of energy into the magnetosphere (for southward turnings), or a sudden energy release in the form of a magnetospheric substorm (for northward turnings) can occur [*Tsurutani et al.*, 2011].

The advent of space-based UV imaging revealed the fascinating response of aurorae to the passage of shocks, as researchers were able to observe the dynamics of the entire oval at once [e.g., *Craven et al.*, 1986]. Data from later UV imaging platforms such as the Polar Ultraviolet Imager (UVI) and Imager for Magnetopause-to-Aurora Global Exploration (IMAGE) have produced image sequences of higher fidelity and time resolution than ever before [e.g., *Vorobjev et al.*, 2001], and in the latter case, the ability to unambiguously separate the proton and electron auroral components of shock aurora and their asymmetries between the dawn- and dusk sides of the auroral oval. [e.g., *Meurant et al.*, 2003, 2004].

Space-based observations revealed that the shock auroral brightening in most cases appears first near local noon and then propagates along the dusk and dawn flanks of the oval towards the nightside [e.g., *Spann et al.*, 1998, *Brittnacher et al.*, 2000]. However, after the initial brightening, different propagation speeds have been observed. One observed type of near-instantaneous (~few minutes or less) auroral enhancement over part

of [*Chua et al*., 2001] or the entire auroral oval [*Zesta et al*., 2000; *Boudouridis et al*., 2003; *Meurant et al*., 2003], is attributed to fast Alfvén waves propagating across magnetic flux tubes [see discussion in e.g., *Kozlovsky et al*., 2007; *Motoba et al*., 2009]. The second type is a slower response, observed as a continuous propagation of auroral enhancement along the oval, reaching magnetic midnight in less than about 20 minutes. The propagation speeds are reported to be in the range of 6–11 km/s in the ionosphere, which, when mapped to the magnetospheric equator, roughly coincide with the speed of the shock passage in the magnetosheath and along the magnetopause [*Zhou and Tsurutani*, 1999]. Furthermore, the propagation of electron and proton shock aurora in some slow-response cases has been found to be different between the dawn and dusk sides, following the relative quiescent prevalence of electron and proton trapped particle populations as a function of MLT [*Meurant et al*., 2003].

Ground-based observations of shock auroral occurrence have added needed detail to complement advances using only space-based imagery. In addition to being able to refine the timing of shock auroral propagation with higher temporal resolution, such measurements possess the ability to spectrally and spatially discriminate between different auroral forms, thereby giving insight into their magnetospheric source regions and related particle acceleration physics.

One example is the identification of discrete dayside auroral arcs, found along the polar edge of the auroral oval and near the open/closed field line boundary, and a region of diffuse aurora more equatorward on closed field lines. The discrete auroral component is created by lower energy electron precipitation along highly structured field-aligned currents, as illustrated by a higher ratio of λ630.0 nm to λ557.7 nm emissions. The magnetospheric phenomena producing these auroral forms are thought to be magnetopause perturbations, magnetic shearing, and/or kinetic Alfvén waves generated by magnetic merging. By contrast, the diffuse precipitation is believed to occur by increased pitch angle scattering into an enlarged loss cone, owing to increased temperature anisotropy, loss cone instability, and wave-particle interactions [*Zhou et al*., 2003, 2009]. An illustration of the different processes that give rise to both discrete and diffuse shock aurora are shown in Figure 14.

In one event, proton and electron aurorae were detected in the diffuse region, yet with a different propagation speed and a two-pulse proton aurora onset pattern [*Motoba et al*., 2009]. The relative occurrence of proton and electron aurora in the previous example, observed both from ground and space, is shown in Figure 15. The different propagation

speeds between electron and proton shock aurora are also reported in Paper V. More recently, *Liu et al*. [2011] published an instance of auroral intensity *decreasing* during increased P_{ram} associated with a shock passage, which was attributed to a postnoon downward Birkeland current, as modelled by *Araki* [1994].

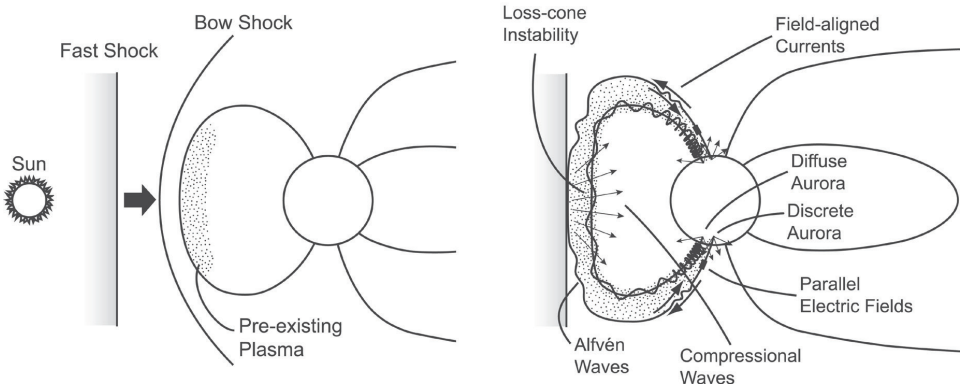

Figure 14. Depiction some possible physical mechanisms that give rise to discrete and diffuse shock aurora. After *Zhou et al* [2003].

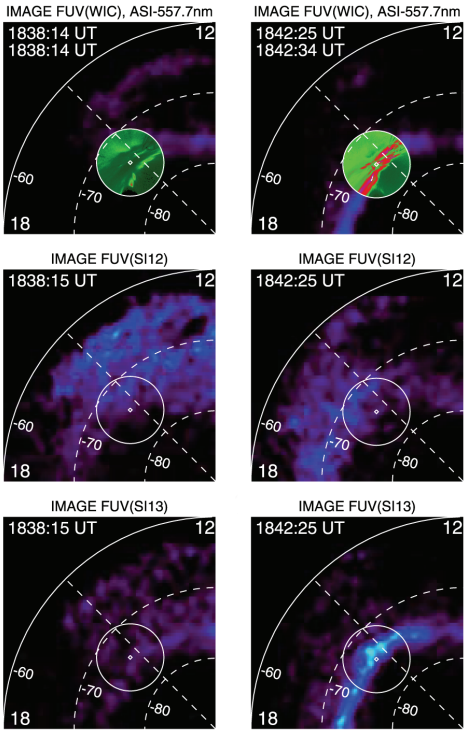

Figure 15. Shock aurora observed by IMAGE and an all-sky imager at South Pole Station. Top row: broadband aurora from Wideband Imaging Camera (WIC); middle row: SI12 images of hydrogen (proton) aurora at Ly α; bottom row: SI13 images of electron aurora. After *Motoba et al*. [2009.]

2. Motivation

Many studies of the relationship between solar wind / dayside magnetosphere interactions and dayside auroral phenomena have concentrated on IMF control of magnetospheric merging and the corresponding auroral response [*Sandholt et al*., 1986, 1998; *Onsager and Elphic*, 1996, and references therein; *Deehr et al*., 1998]. In general, this suite of research topics has been approached with many perspectives and experimental techniques, including but not limited to: rocket-borne measurements of auroral particles, photons and electromagnetic fields, satellite-based measurements of the same, ground-based magnetic, sounder and radar observations of auroral plasma motion and dynamics, and ground-based optical imaging and spectroscopy of proton and electron aurora.

As mentioned in Section 1.2.2, there was no mistaking the circumstantial evidence of the similar temporal occurrence of PMAFs to the repetition rate of FTEs at the magnetopause. And yet, no single theory has been found to consistently explain the causal relationship between dayside electron arcs and PMAFs to FTEs. Since the study of dayside proton precipitation and auroral hydrogen emissions is supported by theory that does explain their relationship to dayside merging, they were chosen to further separate spatial from temporal variations in dayside proton aurora and their context with respect to PMAFs and FTEs [*Deehr*, 2002].

Much was learned previously about the detailed nature of dayside proton aurora in and near the cusp. Two examples are: highly time-resolved observations of the pulsed temporal nature of dayside hydrogen emissions [*Sigernes et al*., 1996], and sudden increases in precipitating proton energy associated with increases in the magnetopause-merging rate [*Deehr et al*., 1998]. These studies were performed using a single observatory.

The ion velocity filter effect, initially measured by satellites high in the magnetospheric mantle [*Rosenbauer et al*., 1975; *Haerendel*, 1975], was later observed in the dayside auroral precipitation zone [e.g., *Newell and Meng*, 1988; *Newell et al*., 1991]. Figure 16 shows ion energy spectra obtained with a Defense Meteorological Satellite Progam (DMSP) satellite in low earth orbit (bottom panel, near 12:46:00 UT). The spectra clearly depict the signature of increasing ion energy with decreasing latitude. But the effect had yet to be observed optically from the ground. Quantifying the velocity filter effect from the ground requires auroral hydrogen measurements from multiple observatories in order to

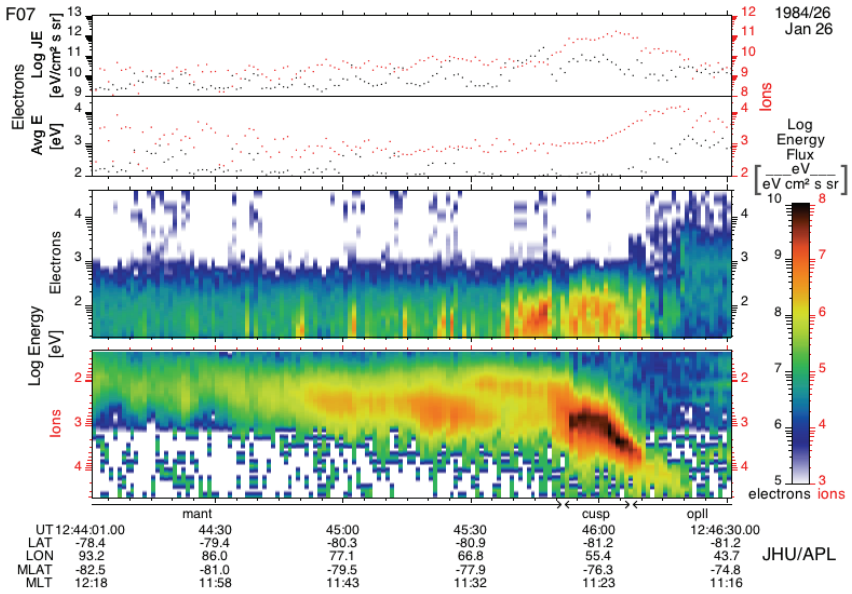

Figure 16. Ion velocity filter effect in the cusp, as measured by DMSP F7 particle detectors. After *Newell et al*. [1991].

observe the difference in Doppler shift, and thus the characteristic energy of the H^+/H particle population.

Why the ability to monitor the ion energy dispersion from the ground is important is a matter of the spatio-temporal difference between ground-based and low earth orbit satellite measurements. For example, particle sensors onboard the DMSP satellites produce high-fidelity measurements of electron and ion energy flux and differential energy spectra. The low altitude orbit results in snapshot-like observations of the region of interest, in this case, the cusp. In order to observe the rate of change of any parameters determined by DMSP over a period of more than a couple of minutes, one must wait until the next orbital period (~100 minutes). On the contrary, ground-based observatories slowly rotate into and out of the cusp, and can provide continuous observations for up to hours at a time.

Regarding proton and electron shock aurora, by far the majority of studies investigating these phenomena use satellite-based observations from which to draw scientific findings. This was done presumably owing to the large number of available observations, and the fact that ground-based optical observatories only operate during winter months and are plagued by cloud cover. As such, dayside ground-based optical observations of a shock-aurora onset at MLTs close to the initial brightening location are exceedingly rare [e.g.,

Sandholt et al., 1998; *Kozlovsky et al*., 2005; *Motoba et al*., 2009; *Vorobjev et al*., 2009; *Zhou et al*., 2009].

Such ground-based endeavours contribute needed spatial, temporal and often spectral detail that is often lacking in solely satellite-based studies. The ground-based studies mentioned above have all revealed heretofor unobserved details in shock-aurora evolutions such as the relative location of diffuse and discrete aurora [*Sandholt et al*., 1998; *Vorobjev et al*., 2009; *Zhou et al*., 2009], and motion of the dayside auroral oval boundaries, in cluding the shock's affect on the luminosity distribution within the oval [*Kozlovsky et al., 2005*].

However, not all ground-based shock aurora works use data from instrumentation capable of discriminating between proton and electron aurora. Clearly, being able to discriminate between the two particle populations by the aurora they produce can yield new physical insight into the magnetospheric source populations and their resoponse to solar wind shocks and pressure pulses. The technique also can help constrain the various proposed theoretical processes by which shocks accelerate particles and produce auroral precipitation (cf. Figure 14). Finally, the above-mentioned studies and others have used no more than two ground-based observatories to observe shock aurora, and have sampled a limited range of MLT focused near magnetic noon. A set of distributed, ground-based observations can sample the effects of the passing shock on different auroral oval sectors.

3. Summary of Papers

Five papers are presented in this work. The first two papers describe procedures and methods used to perform intensity calibrations of both narrow-field instruments, such as the spectrometers used to acquire hydrogen spectra, and commercially available Digital Single Lens Reflex (DSLR) cameras. For comparisons to other complementary datasets, all data presented in the remaining papers are calibrated absolutely with respect to intensity and wavelength using the techniques described.

The following two papers describe results from the Protonics project, which is an experiment involving the measurement of dayside auroral hydrogen emissions from two locations on Svalbard collinear in magnetic longitude: Longyearbyen (LYR) and Ny-Ålesund (NYA). These papers are case studies of auroral hydrogen spectral measurements, applied to the characterization of cusp auroral proton populations and their source region dynamics. The main result from these studies is that the ion velocity filter effect can be observed, with sufficiently high fidelity, from a pair of ground-based observatories spaced ~100 km apart. Energy differences in the precipitating H^+/H population, and their development in time, are observable for much longer than a brief observation from a passing low earth orbiting satellite.

The final paper investigates the relative contributions of proton and electron precipitation to shock aurorae. This study includes distributed ground-based optical observations covering much of the boreal auroral zone using five multichannel meridian scanning photometers. Data from the photometers are used to intuit the spatio-temporal occurrence of shock-induced proton and electron aurora enhancement with high resolution. Ultraviolet imagery from the Polar spacecraft provides contextual data of the entire boreal auroral oval during the shock passage. An interesting finding is that a two-pulse shock aurora onset, involving both precipitating protons and electrons, was observed in two cases. One of the cases is a prenoon observation that suggests field-aligned currents opposite to those of a previously reported postnoon event.

There are two themes that link the final three observational papers. The first is technique, as the experiments all employ distributed, ground-based observations of auroral hydrogen emissions. The second, more important, theme is the investigation of ionospheric and auroral effects of solar wind interaction with the magnetosphere. Having shown the relationship between auroral hydrogen emissions to the strength and orientation

of the IMF (Papers III–IV), the next logical step was to investigate this relationship to other IMF conditions. In the case of Paper V, the purpose is to explore the response of the auroral oval to increases in the solar wind dynamic pressure in the form of fast shocks.

Paper I: Sigernes, F., J. M. Holmes, M. Dyrland, D. Lorentzen, S. Chernous, T. Svenøe, J. Moen, and C. S. Deehr (2007), Absolute calibration of optical devices with a small field of view, *J. Opt. Technol.*, *74,* 669-674.

The method by which spectrometers, such as those used in the Protonics project, are calibrated absolutely with respect to intensity is described. Specifically, this paper discusses a method suitable for optical instruments with small fields of view (FOV, i.e. $\lesssim$ 15 degrees full angle). A determination of the ratio of electronic or digital counts output to the number of input photons is an absolute intensity calibration. The setup of the UNIS calibration laboratory is given, and the mathematical framework of the calibration process using a tungsten lamp of known radiance and a Lambertian diffuser screen is outlined. The method is exemplified for a spectrometer calibration and a secondary lamp certification. Finally, a technique to control the exitance of the known source without varying its spectral response is illustrated using the variation of brightness at the detector with distance between the lamp and the Lambertian screen.

Paper II: Sigernes, F., J. M. Holmes, M. Dyrland, D. A. Lorentzen, T. Svenøe, K. Heia, T. Aso, S. Chernouss, and C. S. Deehr (2008), Sensitivity calibration of digital colour cameras for auroral imaging, *Opt. Express, 16*, 15623-15632.

This paper is an application of the concepts discussed in Paper I, only applied to commercially available Digital Single Lens Reflex (DSLR) cameras. Narrow-band light produced by a monochromator is used as a source, and is varied in wavelength such that a library of nearly monochromatic lines from 400 to 700 nm is produced. An intensity calibrated spectrometer and a DSLR camera both image the output projected onto a diffusing screen. Details and caveats on the procedure used to calculate the spectral responsivity are given, and the result is calculated for two different Nikon cameras. When DSLR images are separated into their component colours, the red and green portions have adequate spectral sensitivity to detect the common auroral emissions of λ630.0 (red) and λ557.7 nm (green) during both dayside and nightside

conditions. For ideal detection capabilities, the red and green spectral responsivities should be shifted around 30.0 and 40.0 nm, respectively.

Paper III: Holmes, J. M., B. V. Kozelov, F. Sigernes, D. A. Lorentzen, and C. S. Deehr, Dual site observations of dayside Doppler-shifted hydrogen profiles: preliminary results. *Can. J. Phys.*, 86(5): 691–698 (2008), doi:10.1139/P08-026.

This paper describes the initial case study of distributed measurements of auroral hydrogen spectra on Svalbard. Simultaneous spectra from both LYR and NYA are presented for two different days. A detailed process of fitting simulated hydrogen Doppler profiles generated by a Monte-Carlo algorithm is used to estimate the precipitating proton energy. In addition, a robust method used to fit the contaminating OH (6-1) airglow band ensures isolated Balmer alpha (H_α) emissions before fitting modelled profiles. Balmer beta (H_β) spectra, which are more easily contaminated by Rayleigh-scattered twilight, are isolated using a technique where a normalized pure twilight spectrum is subtracted from the data. Energies estimated between the two stations were compared and emissions from lower latitudes were found to be of slightly higher energy when averaged over approximately two hours. This preliminary result supports the ion velocity filter paradigm, which predicts such a latitudinal energy difference because of spatial ion energy dispersions owing to an acceleration process taking place on tailward-swept newly reconnected field lines.

Paper IV: Holmes, J. M., B. V. Kozelov, N. J. Peters, C. S. Deehr, D. A. Lorentzen, and F. Sigernes (2009), Ion velocity filter effect observed in dayside hydrogen aurora, *Geophys. Res. Lett.*, 36, L23101, doi:10.1029/2009GL040972.

This study is a continuation of the experiment whose initial results are presented in Paper III. In the previous paper, H_α spectra at NYA were compared with H_β at LYR. Data from a newly deployed Ebert-Fastie spectrometer at LYR allow for the more straightforward comparison of H_α at both locations. A 45-minute period of strong cusp proton aurora was analysed in a manner similar to that in Paper III. In this case, a statistically significant energy difference was found throughout the period. In addition, the high signal-to-noise ratio in both datasets resulted in energy uncertainties small enough to sufficiently time-resolve the energy difference and its evolution. This is the

first statistically significant ground-based measurement of the ion velocity filter effect, previously measured by both low- and high-altitude satellites in the cusp and mantle regions of the magnetosphere. Finally, the energy difference over the period increased with time, which is indicative of a decreasing merging rate at the reconnection site.

Paper V: Holmes, J. M., M. G. Johnsen, C. S. Deehr, X.-Y. Zhou, and D. A. Lorentzen, Circumpolar ground-based optical measurements of proton and electron shock aurora, *J. Geophys. Res. Space Physics, 119,* 3895–3914, doi:10.1002/2013JA019574.

Meridian scanning photometer (MSP) data are combined with global ultraviolet images from the Polar Ultraviolet Imager instrument to estimate the timing and propagation speed of shock auroras previously studied using solely space-based ultraviolet auroral imagery. The multispectral nature of the MSPs, including the presence of a Balmer beta channel, enables the discrimination between proton and electron aurora. Following a near-magnetic noon onset, the occurrence of auroral emissions created by shocked precipitating protons and electrons is observed to propagate tailward, along the auroral oval with speeds of several km/s, consistent with the shock propagation speed in the solar wind. In two cases, shock aurora propagation speeds along the auroral oval determined from satellite imagery are confirmed, to within calculated uncertainties, with ground-based timing. The majority of instruments detect low-energy discrete auroral arcs poleward of diffuse, higher-energy aurora. Evidence of a previously reported two-pulse proton aurora shock onset is detected at some, but not all, locations.

4. Outstanding Problems and Future Work

While the most general properties and physics of auroral proton precipitation have been worked out decades ago, there remain some details that still elude explanation. For example, the red-shifted wing of the auroral hydrogen Doppler profile is now accepted to be the optical manifestation of *upward* moving protons, also known as albedo flux.

While the red-shifted wing was not a critical part of the analysis in Papers III and IV, which focused on the ion velocity filter effect of *downward* moving H^+/H particles, the Monte Carlo model still fitted the entire Doppler profile. Data-model discrepancies contributed to the overall uncertainty calculation for the downward-moving H^+/H characteristic energy. What is more, H^+/H albedo flux is still worth exploring in its own right to further complete the body of knowledge about proton aurora.

Currently, there is disagreement regarding the physical processes by which albedo flux is created. Some modelling efforts have recreated physically reasonable fluxes in agreement with observations by using a fairly large collisional angular redistribution at low energies (1 keV or less). However, this assumption does not agree with current information about relevant cross sections. As an alternative, detailing the scattering reactions for specific excited states is more realistic, as certain excited hydrogen states naturally lend themselves to large angle scattering [*Kozelov and Holmes*, 2008], ultimately creating a source of albedo flux. At the time of writing, the theoretical basis for this adaptation has been worked out but not implemented in existing models.

Regarding continuing research on the ion velocity filter effect, and more generally the relationship between cusp proton aurora, its electron counterpart, and dayside magnetospheric boundary layer dynamics, several challenging but immediately possible variations should be undertaken. The first and most obvious one would be to present more cases of the velocity filter effect, as observed in Papers III and IV. In the event of positive IMF B_z, the deduced H^+/H energy dispersion should be the opposite sense of that reported in Papers III and IV. Again, this has not been observed from the ground.

A useful addition would be to include *in situ* particle data from a satellite conjunction, which could be used to constrain the assumptions about the top-of-atmosphere precipitating proton flux (that is, energy and pitch angle distribution functions) for modelling. There is, however, some luck involved in obtaining good ground-based data during a fortuitously timed conjunction.

Next, the determined energy dispersion of H^+/H particles between a pair of ground stations can be used to make an estimate of the merging rate at the magnetopause. This rate can then be compared with other estimates determined by other means, for example using the SuperDARN network of coherent-scatter radars, high-latitude incoherent-scatter radars such as EISCAT, and the inclusion of relevant space-based measurements [e.g., *Lockwood et al*., 2005; *Chisham et al*., 2008 and references therein].

As scientific imaging technology matures, a pair of meridian-imaging spectrographs could eventually replace the photometer-based Ebert-Fastie spectrometers used in cusp hydrogen aurora measurements. Though the required sensitivity would still necessitate large apertures, dynamic binning on the focal plane arrays (for example, using only ~10-20 pixels along the spatial dimension) would allow for many common-volume measurements of adequate spectral resolution.

Finally, further investigation into the relative occurrence of proton and electron shock aurora is encouraged. While at least one study discriminated between proton and electron shock aurora using satellite-based imaging [*Motoba et al*., 2009], the same capability was not employed in the ground-based measurements. High sensitivity, high time resolution imaging of emissions (be they images or meridian scans) is likely to reveal more information and detail about the relative location of proton precipitation, when placed in context with Ly-alpha images from space.

5. References

Araki, T. (1994), A physical model of geomagnetic sudden commencement, in *Solar Wind Sources of Magnetospheric Ultra-Low-Frequency Waves, Geophys. Monogr. Ser.*, vol. 81, edited by M. J. Engebretson, K. Takahashi, and M. Scholer, 183 pp., AGU, Washington, D. C.

Baker, D. J., and G. J. Romick (1976), The Rayleigh: interpretation of the unit in terms of column emission rate of apparent radiance expressed in SI units, *Appl. Opt., 15*, 1966-1968.

Bass, M., Van Stryland, E. W., Williams, D. R., Wolfe, W. L. (1995), *Handbook of Optics*, Volumes I & II, McGraw-Hill, New York.

Basu, B., D. T. Decker, and J. R. Jasperse (2001), Proton transport model: a review, *J. Geophys. Res., 106*(A1), 93-105.

Basu, B., J. R. Jasperse, D. J. Strickland and R. E. Daniell (1993), Transport-theoretic model for the electron-proton-hydrogen atom aurora, 1. Theory, *J. Geophys. Res., 98*, 21017.

Borovkov, L. P., B. V. Kozelov, L. S. Yevlashin, S. A. Chernouss (2005), Variation of auroral hydrogen emission near substorm onset, *Ann. Geo., 23*, 1623-1635.

Boyd, R. W. (1983), *Radiometry and the Detection of Optical Radiation*, Wiley, New York.

Brittnacher, M., M. Wilber, M. Fillingim, D. Chua, G. Parks, J. Spann, G. Germany (2000), Global auroral response to a solar wind pressure pulse. *Adv. Space Res. 25,* 1377–1385.

Burnett, C. http://en.wikipedia.org/wiki/File:Bayer_pattern_on_sensor.svg (2006), licensed under Creative Commons, restrictions: share-alike, attribution.

Chamberlain, J. W. (1954a), The Excitation of Hydrogen in Aurorae, *Astrophys. J., 120*, 360–366.

Chamberlain, J. W. (1954b), On the Production of Auroral Arcs by Incident Protons, *Astrophys. J., 120*, 566–571.

Chamberlain, J. W. (1957), On a Possible Velocity Dispersion of Auroral Protons, *Astrophys. J., 126*, 245-252.

Chamberlain, J. W. (1961), *Physics of the aurora and airglow*, Academic Press, New York.

Chang, G. W., and Y. C. Chen (2001), Spectral Responsivity Estimator for Colour Vision Systems: Filter Selection and Noise Effect, Proceedings of National Sci. Council, Part A , vol. 25, no.2, pp. 115 – 126.

Chisham, G., M. P. Freeman, G. A. Abel, M. M. Lam, M. Pinnock, I. J. Coleman, S. E. Milan, M. Lester, W. A. Bristow, R. Greenwald, G. J. Sofko, J.-P. Villain (2008), Remote sensing of the spatial and temporal structure of the magnetopause and magnetotail reconnection from the ionosphere, *Rev. Geophys., 46,* RG1004, doi:10.1029/2007RG000223.

Craven, J. D., L. A. Frank, C. T. Russell, E. E. Smith, R. P. Lepping (1986), Global auroral responses to magnetospheric compressions by shocks in the solar wind: two case studies, in: Kamide, Y., Slavin, J.A. (Eds.), *Solar Wind-Magnetosphere Coupling*. Terra Scientific, Tokyo, pp. 367–380.

Davidson, G. T. (1965), Expected spatial distribution of low-energy protons precipitated in the auroral zones, *J. Geophys. Res., 70*, 1061-1068.

Decker, D. T., B. V. Kozelov, B. Basu, J. R. Jasperse, and V. E. Ivanov (1996), Collisional degradation of the proton-H atom fluxes in the atmosphere: A comparison of theoretical techniques, *J. Geophys. Res., 101*, 26 947–26 960.

Deehr, C. (1994), Ground-based optical observations of hydrogen emissions in the auroral substorm. *Proc. 2nd Int'l Conf. on Substorms. University of Alaska Fairbanks, Geophysical Institute*, 229-236.

Deehr, C. S. (2002), Thirty-three years of auroral morphology with Alv Egeland across the Pole, Egeland Symposium on Auroral and Atmospheric Research. Moen, J. and J. Holtet (Eds.), Department of Physics, University of Oslo.

Deehr, C. S., D. A. Lorentzen, F. Sigernes, R. W. Smith (1998): Dayside auroral hydrogen emission as an aeronomic signature of magnetospheric boundary layer processes. *Geophy. Res. Lett., 25* (12), 2111- 2114.

Deehr, C. S., D. Lummerzheim (2001), Ground-based optical observations of hydrogen emission in the auroral substorm. *J. Geophys. Res., 106*(A1), 33-44.

Derblom, H. (1975), Observed characteristics of polar cleft H_α and OI emissions, *Planet. Space Sci., 23*, 1053-1058.

Dungey, J. W. (1961), Interplanetary magnetic field and the auroral zones, *Phys. Rev. Lett.*, 6, 47–48, doi:10.1103/PhysRevLett.6.47.

Eather, R. H. (1966), Redshift of auroral hydrogen profiles, *J. Geophys. Res., 71*, 5027.

Eather, R. H. (1967), Auroral proton precipitation and hydrogen emissions, *Rev. Geophys., 5*, 207-285.

Eather, R. H. (1969), Latitudinal distribution of auroral and airglow emissions: the 'soft' auroral zone, *J. Geophys. Res., 74(1)*, 153-158.

Eather, R. H. (1988), Results from Antarctic optical studies, *Rev. Geophys., 26*, 579–590, doi:10.1029/RG026i003p00579.

Eather, R. H., and Burrows, K. M. (1966), Excitation and ionisation by auroral protons, *Austral. J. Phys., 19*, 309.

Eather, R. H., and F. Jacka (1966), Auroral hydrogen emission, *Aust. J. Phys., 19*, 241.

Edgar, B. C., W. T. Miles, and A. E. S. Green (1973), Energy deposition of protons in molecular nitrogen and applications to proton auroral phenomena, *J. Geophys. Res., 78*, 6595.

Edgar, B. C., H. S. Porter, and A. E. S. Green (1975), Proton energy deposition in molecular and atomic oxygen and applications to the polar cap, *Planet. Space Sci., 23*, 787.

Fang, X., A. J. Ridley, M. W. Liemohn, J. U. Kozyra, and D. S. Evans (2007), Global 30-240 keV proton precipitation in the 17-18 April 2002 geomagnetic storms: 3. Impact on the ionosphere and thermosphere, *J. Geophys. Res., 112*, A07310, doi:10.1029/2006JA012144.

Frey, H. U. (2007), Localized aurora beyond the auroral oval, *Rev. Geophys., 45*, RG1003, doi:10.1029/2005RG000174.

Fasel, G. (1995), Dayside poleward moving auroral forms: A statistical study. *J. Geophys. Res.*, 10011891.

Galand, M., J. Lilensten, W. Kofman and R. B. Sidje (1997), Proton transport in the ionosphere, 1: Multi-stream approach of the transport equations, *J. Geophys. Res., 102*, 22261-22272.

Galand, M., J. Lilensten, W. Kofman and D. Lummerzheim (1998), Proton transport model in the ionosphere: 2. Influence of magnetic mirroring and collisions on the angular redistribution in a proton beam, *Ann. Geophys., 16*, 1308-1321.

Galand, M., and A. D. Richmond (1999), Magnetic mirroring in an incident proton beam, *J. Geophys. Res., 104*, 4447-4455.

Galand, M., J. Baumgardner, D. Pallamraju, S. Chakrabarti, U. P. Løvhaug, D. Lummerzheim, B. S. Lanchester, and M. H. Rees (2004), Spectral imaging of

proton aurora and twilight at Tromsø, Norway, *J. Geophys. Res., 109*, A07305, doi:10.1029/2003JA010033.

Galand, M., and S. Chakrabarti (2006), Proton aurora observed from the ground, *J. Atmos. Sol. Terr. Phys., 68*, 1488–1501, doi:10.1016/j.jastp.2005.04.013.

Galperin, Y. I., R. A. Kovrazhkin, Y. N. Ponomarev, J. Crasnier, and J. A. Sadaud (1976), Pitch angle distributions of auroral protons, *Ann. Geophys., 32*, 109.

Gartlein, C. W. (1950), Auroral spectra showing broad hydrogen lines, *Trans. Am. Geophys. Union, 31*, 18–20.

Gérard, J.-C., B. Hubert, D. V. Bisikalo, and V. I. Shematovich (2000), A model of the Lyman-α line profile in the proton aurora, *J. Geophys. Res., 105*, 15795–15806.

Gérard, J.-C., B. Hubert, M. Meurant, V. I. Shematovich, D. V. Bisikalo, H. Frey, S. Mende, G. R. Gladstone, and C. W. Carlson (2001), Observation of the proton aurora with IMAGE FUV imager and simultaneous ion flux in situ measurements, *J. Geophys. Res., 106*, 28939-28948.

Gérard, J.-C., V. I. Shematovich, D. V. Bisikalo, and D. Lummerzheim (2005), A Monte Carlo model of auroral hydrogen line profiles, *Ann. Geo., 23*, 1473-1480.

Haerendel, G. (1975), Die Spur der Magnetopause in Der Magnetosphäre, *Astron. Gesell. Mitt.*, 35, 165-181.

Hardy, D., M. Gussenhoven, and E. Holeman (1985), A Statistical Model of Auroral Electron Precipitation, J. Geophys. *Res., 90*(A5), 4229-4248.

Henriksen, K. (1979), Variations or proton energy and pitch angle spectra in the upper atmosphere, *J. Atm. Terr. Phys., 41*, 633-641.

Henriksen, K., N. I. Fedorova, G. F. Totunova, C. S. Deehr, G. J. Romick, and G. G. Sivjee (1985), Hydrogen Emissions in the Polar Cleft, *J. Atmos. Terr. Phys*, *47*(11), 1051-1056.

Hunten, D. M., F. E. Roach, and J. W. Chamberlain (1956), A photometric unit for the airglow and aurora, *J. Atm. Terr. Phys., 8*, 345-346.

Iglesias, G., and R. R. Vondrak (1974), Atmospheric spreading of protons in auroral arcs, *J. Geophys. Res., 79*, 280–282.

Jasperse, J. R., and B. Basu (1982), Transport theoretic solutions for auroral proton and H atom fluxes and related quantities, *J. Geophys. Res., 87*, 811.

Jasperse, J. R. (1997), Transport theoretic solutions for the beam-spreading effect in the proton-hydrogen aurora, *Geophys. Res. Lett., 24*, 1415-1418.

Johnsen, M. G., and D. A. Lorentzen (2012), A statistical analysis of the optical dayside open/closed field line boundary, *J. Geophys. Res., 117*, A02218, doi:10.1029/2011JA016984.

Johnstone, A. D. (1972), The spreading of a proton beam by the atmosphere, *Planet. Space Sci., 20*, 292–295.

Kozelov, B. V. (1993), Influence of the dipolar magnetic field on transport of proton-H atom fluxes in the atmosphere, *Ann. Geophys.*, *11*, 697.

Kozelov, B. V. (1996), Calculation of H_β in aurora. Comparison with observations, *Geomag. Aeron., 34*, 5, 86-90.

Kozelov, B. V., and J. M. Holmes (2008), Angle scattering and forming the hydrogen Doppler profile in proton aurora, "Physics of Auroral Phenomena", *Proc. XXXI Annual Seminar*, Apatity, Kola Science Centre, Russian Academy of Sciences, 153-156.

Kozelov B. V., and Ivanov V. E. (1992), Monte-Carlo calculation of proton-hydrogen atom transport in N_2, *Planet. Space Sci., 40*, 1503-1511.

Kozlovsky, A., M. Meurant, and T. Turunen (2007), Changes of dayside auroral distribution caused by a solar wind pressure pulse and associated interplanetary magnetic field disturbances, *Ann. Geophys., 25*, 929-940, doi:10.5194/angeo-25-929-2007.

Lambert, J. H. (1760), "Photometria, sive de mensura et gradibus luminis colorum et umbrae", Augsburg. German trans. by E. Anding in Ostwald's "Klassiker d. Exacten Wissenschaften" (Engelmann, Leipzig, 1892), 324.

Lanchester, B. S., M. Galand, S. C. Robertson, M. H. Rees, D. Lummerzheim, I. Furniss, L. M. Peticolas, H. U. Frey, J. Baumgardner, and M. Mendillo (2003), High resolution measurements and modelling of auroral hydrogen emission line profiles, *Ann. Geophys., 21*, 1629-1643.

Lanchester, B. S., D. Lummerzheim, M. H. Rees, M. Galand, J. Baumgardner, and F. Rich (2003), Proton and electron precipitation over Svalbard – first results from a new imaging spectrograph (HiTIES), Proc. of the 28th optical meeting, edited by K. U. Kaila, J. R. T. Jussila, and H. Holma, *Sodankylä Geophysical Observatory Publications, 92*, 33–36.

Lilensten, J., and P.-L. Blelly (2002), The TEC and F2 parameters as tracers of the ionosphere and thermosphere, *J. Atmo. Sol. Terr. Phys., 64*, 775-793.

Liu, J. J., H. Q. Hu, D. S. Han, T. Araki, Z. J. Hu, Q. H. Zhang, H. G. Yang, N. Sato, A. S. Yukimatu, and Y. Ebihara (2011), Decrease of auroral intensity associated with reversal of plasma convection in response to an interplanetary shock as observed over Zhongshan station in Antarctica, *J. Geophys. Res.*, *116*, A03210, doi:10.1029/2010JA016156.

Lockwood, M., and M. Smith (1989), Low-Altitude Signatures of the Cusp and Flux Transfer Events, *Geophys. Res. Lett.*, *16* (8), 879-882.

Lockwood, M., W. F. Denig, A. D. Farmer, V. N. Davda, S. W. H. Cowley, H. Luhr (1993), Ionospheric signatures of pulsed reconnection at the Earth's magnetopause, *Nature*, 361, 424-428.

Lockwood, M., J. Moen, A. P. van Eyken, J. A. Davies, K. Oksavik, I. W. McCrea (2005), Motion of the dayside polar cap boundary during substorm cycles: I. Observations of pulses in the magnetopause reconnection rate, *Ann. Geo, 23,* 3495-3511, doi:10.5194/angeo-23-3495-2005.

Lorentzen, D. (2000), Latitudinal and longitudinal dispersion of energetic auroral protons, *Ann. Geo., 18*, 81-89.

Lorentzen, D. A., C. S. Deehr, J. I. Minow, R. W. Smith, H. C. Stenbaek-Nielsen, F. Sigernes, R. L. Arnoldy, K. Lynch (1996), SCIFER: Dayside auroral signatures of magnetospheric energetic electrons. *Geophys. Res. Lett., 23*(14), 1885-1888.

Lorentzen, D. A., and J. Moen (2000), Auroral proton and electron signatures in the dayside aurora, *J. Geophys. Res.*, *105* (A6), 12733-12745.

Lorentzen, D., F. Sigernes, C. S. Deehr (1998), Modeling and observations of dayside auroral hydrogen Doppler profiles, *J. Geophys. Res., 103*, 17479-17488.

Lummerzheim, D., and M. Galand (2001), The profile of the hydrogen H_β emission line in proton aurora, *J. Geophys. Res., 106*, 23–31, doi:10.1029/2000JA002014.

McNeal, R. J., and J. H. Birely (1973), Laboratory studies of collision of energetic H^+ and hydrogen with atmospheric constituents, *Rev. Geophys. Space Phys., 11*, 633–692.

Meinel, A.B. (1951), The spectrum of the airglow and the aurora, *Rep. Prog. Phys., 14*, 121–146.

Meurant, M., J.-C. Gérard, B. Hubert, V. Coumans, C. Blockx, N. Østgaard, and S. B. Mende (2003), Dynamics of global scale electron and proton precipitation induced by a solar wind pressure pulse, *Geophys. Res. Lett.*, 30(20), 2032, doi:10.1029/2003GL018017.

Meurant, M., J.-C. Gérard, C. Blockx, B. Hubert, and V. Coumans (2004), Propagation of electron and proton shock-induced aurora and the role of the interplanetary magnetic field and solar wind, *J. Geophys. Res.*, 109, A10210, doi:10.1029/2004JA010453.

Motoba, T., A. Kadokura, Y. Ebihara, H. U. Frey, A. T. Weatherwax, and N. Sato (2009), Simultaneous ground-satellite optical observations of postnoon shock aurora in the Southern Hemisphere, *J. Geophys. Res., 114,* A07209, doi:10.1029/2008JA014007.

Newell, P. T., and C.-I. Meng (1988), The cusp and the cleft/boundary layer: Low-altitude identification and statistical time variation, *J. Geophys. Res.*, *93* (A12), 14549-14556.

Newell, P. T., W. J. Burke, C.-I. Meng, E. R. Sanchez, and M. E. Greenspan (1991), Identification and observation of the plasma mantle at low altitude, *J. Geophys. Res., 96*, A1, 35-45.

Newell, P. T., and C.-I. Meng (1992), Mapping the dayside ionosphere to the magnetopause according to particle precipitation characteristics, *Geophys. Res. Lett.*, *19*, 609.

Nishida, A. (1978), Geomagnetic diagnosis of the magnetosphere, *Physics and Chemistry in Space*, Volume 9, p. 256, Springer-Verlag, New York.

Omholt, A. (1956), Characteristics of auroras caused by angular dispersed protons, *J. Atmos. Terr. Phys., 9*, 18–27.

Onsager, T. G., Elphic, R. C. (1996), Is magnetic reconnection intrinsically transient or steady-state? The Earth's magnetopause as a laboratory. *EOS Trans.,* 77, 26,241.

Palmer, J. M., and B. G. Grant (2009), *The Art of Radiometry*, SPIE Press, ISBN 978-0-819-47245-8.

Parks, G. (2003), Physics of space plasmas: An Introduction, Second Edition, Westview Press, ISBN 0813341302.

Partamies, N., M. Syrjaesuo, and E. Donovan (2007), Using colour in auroral imaging. *Can. J. Phys., 85,* 101–109, doi: 10.1139/P06-090.

Peters, N. (2009), Development and calibration of a DSLR system for auroral studies, Master's thesis, University of Oslo / University Centre in Svalbard. http://www.duo.uio.no/sok/work.html?WORKID=91494&fid=50961

Ponomarev, Y. N. (1976), Intrusion of the monoenergetic monodirectional beams of proton into the high atmosphere (in Russian), *Kosmi. Issled., 14*, 144.

Rayleigh, Lord (Strutt, R. J.) (1930), Absolute intensity of the aurora line in the night sky and the number of atomic transitions, *Proc. Roy. Soc.* (London), A 129, 11-33.

Rees, M. H. (1989), Antarctic upper atmosphere investigations by optical methods, *Planet. Space Sci., 37*, 955–966.

Rosenbauer, H., H. Gruenwaldt, M. D. Montgomery, G. Paschmann, and N. Sckopke (1975), Heos 2 plasma observations in the distant polar magnetosphere – The plasma mantle, *J. Geophys. Res., 80*, 2723–2737.

Russell, C. T., and R. C. Elphic (1978), Initial ISEE Magnetometer Results: Magnetopause Observations, *Space Science Reviews*, *22*, 681-715.

Russell, C. T., and R. C. Elphic (1979), ISEE Observations of Flux Transfer Events at the Dayside Magnetopause, *Geophys. Res. Lett.*, *6* (1), 33-36.

Russell, C. T. (2000), The solar wind interaction with the Earth's magnetosphere: a tutorial, *IEEE Trans. Plasma Sci., 28*(6), 1818-1830, doi:10.1109/27.902211.

Sandholt, P. E., C. S. Deehr, A. Egeland, B. Lybekk, R. Viereck, and G. Romick (1986), Signatures in the Dayside Aurora of Plasma Transfer From the Magnetosheath, *J. Geophys. Res.*, *91* (A9), 10063-10079.

Sandholt, P. E., C. J. Farrugia, J. Moen, Ø. Noraberg, B. Lybekk, T. Sten, and T. Hansen (1998), A classification of dayside auroral forms and activities as a function of interplanetary magnetic field orientation, *J. Geophys. Res., 103*(A10), 23,325–23,345, doi:10.1029/98JA02156.

Sandholt, P. E., W. F. Denig, C. J. Farrugia, B. Lybekk, and E. Trondsen (2002), Auroral structure at the cusp equatorward boundary: Relationship with the electron edge of low-latitude boundary layer precipitation, *J. Geophys. Res., 107*(A9), 1235, doi:10.1029/2001JA005081.

Sigernes, F. (1996), Estimation of initial auroral proton energy fluxes from Doppler profiles, *J. Atmos. Terr. Phys, 58*, 1871-1883.

Sigernes, F., G. Fasel, J. Minow, C. S. Deehr, R. W. Smith, D. A. Lorentzen, L. T. Wetjen, and K. Henriksen (1996), Calculations and ground-based observations of pulsed proton events in the dayside aurora, *J. Atmo. Terr. Phys, 58*, 1281-1291.

Sigernes, F., D. A. Lorentzen, C. S. Deehr, and Henriksen, K. (1994), Calculation of auroral Balmer volume emission height profiles in the upper atmosphere, *J. Atmos. Terr. Phys., 56*, 503.

Simon, C. (2006), Contribution à l'étude des entrées d'énergie solaire dans l'ionosphère : Ions doublement chargés et transport cinétique des protons - Application à la Terre et à Titan, PhD Thesis, Université Joseph-Fourier, Grenoble I, http://tel.archives-ouvertes.fr/tel-00109802/en/.

Simon, C., J. Lilensten, J. Moen, J. M. Holmes, Y. Ogawa, K. Oksavik, and W. F. Denig (2007), TRANS4: a new coupled electron/proton transport code – comparison to observations above Svalbard using ESR, DMSP and optical measurements, Ann. Geo., 25, 661-673.

Strickland, D. J., R. E. Daniell, Jr., J. R. Jasperse, and B. Basu (1993), Transport-theoretic model for the electron-proton-hydrogen atom aurora, 2. Model results, *J. Geophys. Res., 98*, 21533.

Synnes, S. A., F. Søraas, and J. P. Hansen (1998), Monte-Carlo simulations of proton aurora, *J. Atmos. Sol. Terr. Phys., 60*, 1695–1705.

Søraas, F. and K. Aarsnes (1996), Observations of ENA in and near a proton arc, *Geophys. Res. Lett., 23*, 2959–2962.

Søraas, F., H. R. Lindalen, K. Måseide, A. Egeland, T. A. Sten, and D. S. Evans (1974), Proton precipitation and the H_β emission in a postbreakup auroral glow, *J. Geophys. Res., 79*, 1851-1859.

Tsurutani, B. T., G. S. Lakhina, O. P. Verkhoglyadova, W. D. Gonzalez, E. Echer, F. L. Guarnieri (2011), A review of interplanetary discontinuities and their geomagnetic effects, *J. Atmos. Sol. Terr. Phys., 73*, 5-19, doi:10.1016/j.jastp.2010.04.001.

Tsyganenko, N. A. and C. T. Russell (1999), Magnetic signatures of the distant polar cusps: Observations by Polar and quantitative modeling, *J. Geophys. Res., 104*(A11), 24939-24955, doi:10.1029/1999JA900279.

Tuan, R. F., On the Doppler profiles for auroral hydrogen emission (1962), *Astrophys. J., 136*, 283.

Vallance Jones, A. (1974), Aurora, D. Reidel Publishing Company, Dordrecht, Holland.

Vegard, L. (1939), Hydrogen showers in the auroral region, *Nature, 144*, 1089–1090.

Vegard, L. (1948), Emission spectra of night sky and aurora, *Report of the Gassiot Committee, 82*, The Physical Society London.

Vorobjev, V. G., O. I. Yagodkina, D. G. Sibeck, K. Liou, and C.-I. Meng (2001), Polar UVI observations of dayside auroral transient events, *J. Geophys. Res., 106*, 28,897.

Vorobjev, V. G., V. L. Zverev, and O. I. Yagodkina (2009), Response of dayside auroras to abrupt increases in the solar wind dynamic pressure at positive and negative polarity of the IMF BZ component, *Geomagn. Aeron., 49* (6), 746-756.

Wyatt, C. L. (1978), *Radiometric Calibration: Theory and Methods*, Academic Press, New York, 1978.

Yevlashin, L. S. (2000), Hydrogen emission in auroras and the precipitation of auroral protons, *In: "Physics of the near-earth Space", part 3*, Apatity, Kola Science Centre RAS, 500–548.

Zesta, E., H. J. Singer, D. Lummerzheim, C. T. Russell, L. R. Lyons, and M. J. Brittnacher (2000), The effect of the January 10, 1997, pressure pulse on the magnetosphere-ionosphere current system, in *Magnetospheric Current Systems, Geophys. Monogr. Ser.*, vol. 118, edited by S. Ohtani, R. Fujii, M. Hesse, and R. L. Lysak, p. 217, AGU, Washington, D. C.

Zhou, X.-Y. and B. T. Tsurutani (1999), Rapid intensification and propagation of the dayside aurora: Large-scale interplanetary pressure pulses (fast shocks), *Geophys. Res. Lett.*, 26, 1097.

Zhou, X.-Y., R. J. Strangeway, P. C. Anderson, D. G. Sibeck, B. T. Tsurutani, G. Haerendel, H. U. Frey, and J. K. Arballo (2003), Shock aurora, FAST and DMSP observations, *J. Geophys. Res.*, 108(A4), 8019, doi:10.1029/2002JA009701.

Zhou, X.-Y., K. Fukui, H. C. Carlson, J. I. Moen, and R. J. Strangeway (2009), Shock aurora: Ground-based imager observations, *J. Geophys. Res.*, *114*, A12216, doi:10.1029/2009JA014186.

Paper I

Absolute calibration of optical devices with a small field of view

F. Sigernes, F., J. M. Holmes, M. Dyrland, D. Lorentzen, S. Chernous, T. Svenøe, J. Moen, and C. S. Deehr

Published in: Journal of Optical Technology

Citation: Sigernes, F., J. M. Holmes, M. Dyrland, D. Lorentzen, S. Chernous, T. Svenøe, J. Moen, and C. S. Deehr (2007), Absolute calibration of optical devices with a small field of view, *J. Opt. Technol., 74(10)*, 669-674.

Paper II

Sensitivity calibration of digital colour cameras for auroral imaging

F. Sigernes, J. M. Holmes, M. Dyrland, D.A. Lorentzen, T. Svenøe, K. Heia, T. Aso, S. Chernouss, and C. S. Deehr

Published in: Optics Express

Citation: Sigernes, F., J. M. Holmes, M. Dyrland, D. A. Lorentzen, T. Svenøe, K. Heia, T. Aso, S. Chernouss, and C. S. Deehr (2008), "Sensitivity calibration of digital colour cameras for auroral imaging," *Opt. Express, 16*, 15623-15632.

Paper III

Dual site observations of dayside Doppler-shifted hydrogen profiles: preliminary results

J. M. Holmes, B. V. Kozelov, F. Sigernes, D. A. Lorentzen, C. S. Deehr

Published in: Canadian Journal of Physics

Citation: Holmes, J. M., B. V. Kozelov, F. Sigernes, D. A. Lorentzen, and C. S. Deehr, Dual site observations of dayside Doppler-shifted hydrogen profiles: preliminary results. *Can. J. Phys., 86*(5): 691–698 (2008), doi:10.1139/P08-026.

Dual site observations of dayside Doppler-shifted hydrogen profiles: preliminary results

J. M. Holmes[1], B. Kozelov[2], F. Sigernes[1], D. A. Lorentzen[1], C. S. Deehr[3]

[1] The University Centre in Svalbard (UNIS), N-9171 Longyearbyen, Norway

[2] Polar Geophysical Institute, Apatity, Murmansk Region, Russia

[3] Geophysical Institute, University of Alaska, Fairbanks, Alaska, USA

Corresponding author:
Jeffrey M. Holmes
E-mail: jeff.holmes@unis.no

PACS Nos.: 92.60.hw 94.20.Ac, 94.30.Aa

Abstract. Simultaneous optical ground-based observations of auroral Balmer excited hydrogen atoms were performed during the boreal winters of 2002-2003 and 2003-2004 at Ny-Ålesund, Svalbard (NYA 76.26°N 110.98°E geomagnetic) and Longyearbyen, Svalbard (LYR 75.31°N 111.88°E geomagnetic). Balmer α (H_α) with a natural wavelength of 6563 Å was detected at Ny-Ålesund, while Balmer β (H_β) at 4861 Å was measured at Longyearbyen. The emissions are well known to originate from precipitating protons whose charge exchanges with the neutral atmosphere lead to a diffuse, Doppler-shifted emission region. Measurements are made using Ebert-Fastie spectrometers that are located 118 km apart on a line of roughly constant geomagnetic longitude, thus making this configuration suitable for studying the variation of proton energy with geomagnetic latitude, the so-called "velocity filter" effect. For two different days, analysis of the spectrometer data sets was performed, yielding in both cases positive energy differences between LYR and NYA in support of the velocity filter concept. In order to reduce uncertainties in the determined energies obtained from the Doppler profile, distributions of energy difference were constructed using the entire time period (up to 2 h) for each case.

1. Introduction

Although auroral hydrogen emissions owing to proton precipitation are typically not as intense as other emissions resulting from precipitating electrons, they nonetheless are a signature of a significant amount of energy transferred into the Earth's thermosphere. In fact, proton precipitation, the source of auroral hydrogen emissions, can sometimes be the dominant source of energy input in a given auroral event [*Rees*, 1982]. The diffuse nature of proton precipitation and the associated optical emissions produce a large-scale optical ionospheric footprint of magnetospheric plasma sources [*Lorentzen and Moen*, 2000]. This can be used to map from the ionosphere to dayside magnetopause reconnection sites and characterize the spatial distribution of precipitating ion energy [*Deehr et al.*, 1998].

A beam of protons incident upon the upper atmosphere is initially confined to a magnetic flux tube. Hydrogen atoms are created after a fraction of the proton population undergoes charge exchange reactions with the ambient neutral constituents. The repeated process of charge exchange and stripping produces a mixed proton/hydrogen (H^+/H) population. Newly formed hydrogen atoms, no longer confined to the magnetic field, propagate downward across field lines with pitch angles like the initial protons. Therefore the transverse width of a H^+/H beam increases with decreasing altitude to the region of effective energy dissipation, thus producing the diffuse aspect of proton aurora [*Davidson*, 1965].

Owing to the initial earthward momentum of a H^+/H beam, hydrogen emissions viewed in the magnetic zenith at the ground will be generally Doppler shifted towards shorter wavelengths. This shift was first detected by Vegard during the boreal winter of 1939–1940 [*Vegard*, 1939, 1940]. Further evidence to support the notion that auroral emissions in general are caused by precipitating particles was lent by *Meinel* [1951], *Galperin* [1959], *Yevlashin* [1961], and later *Eather and Jacka* [1966]. The asymmetric Doppler-shifted hydrogen profiles were obtained while observing in the magnetic zenith and the symmetric Doppler-broadened ones while observing in the direction of the magnetic horizon. Only line-of-sight motions of emitting particles produce a net Doppler shift. Therefore, for magnetic zenith profiles only the motion parallel to the magnetic field produces a shift while the gyroscopic motion has no effect. Conversely, when pointing toward the magnetic horizon, only the gyroscopic motions of the H^+/H population produce a broadening which is symmetric about the unshifted line. Several

reviews of progress in the study of auroral hydrogen emissions are given by *Eather* [1967], *McNeal and Birely* [1973], *Eather* [1988], *Rees* [1989], *Yevlashin* [2000] and *Galand and Chakrabarti* [2006].

As the technology required to produce both high resolution instruments and narrow bandpass interference filters improved, a contribution in the observed hydrogen emission profiles shifted to longer wavelengths was observed. Whereas in the past this red-shifted component was thought to be the result of the convolution of wider instrumental functions, recent high resolution measurements with much narrower instrument functions unambiguously measured this "red wing" and determined it to be an attribute of the emission itself [*Lummerzheim and Galand*, 2001; *Lanchester et al*., 2003]. The physical interpretation of such a feature is that there exists a fraction of the H^+/H population propagating upward in the lower thermosphere. The red-shifted component was also reproduced by the numerical model of *Galand et al*. [1998], but with the assumption of very large angular redistribution of the H^+/H population. The cause of this redistribution is noted as being a combination of magnetic mirroring [*Eather*, 1966; *Kozelov*, 1993] and collisional scattering, the latter being more influential at lower altitudes coincident with the hydrogen emission region, which is typically 100-150km depending on the particle energy distribution.

In the case of dayside reconnection at the magnetopause, newly opened field lines, mapping to the dayside cusp, accelerate magnetosheath ions as the field lines are convected antisunward. As this progresses, the fastest ions in the population will arrive at the ionosphere first [*Deehr et al*., 1998]. Assuming a simple geometry, along a given line of magnetic longitude in the ionosphere the energy inferred from the ground for the incoming population will drop while convecting antisunward since the slower particles are arriving later. This process of distributing precipitating particle energy is known as a velocity filter [*Rosenbauer et al*., 1975; *Haerendel*, 1975].

We report on simultaneous measurements made by high resolution Ebert-Fastie (E-F) spectrometers [*Fastie*, 1952; Sivjee *et al*., 1979] at two different locations along a line of nearly constant magnetic longitude. A spectrometer measuring a wavelength region centered around the H_α emission is located at Ny-Ålesund (76.26°N 110.98°E geomagnetic), and one measuring the H_β hydrogen profile is located at Longyearbyen (75.31°N 111.88°E geomagnetic) at the Auroral Station in Adventdalen. Brief instrumental details on the spectrometers, along with the procedure used to isolate

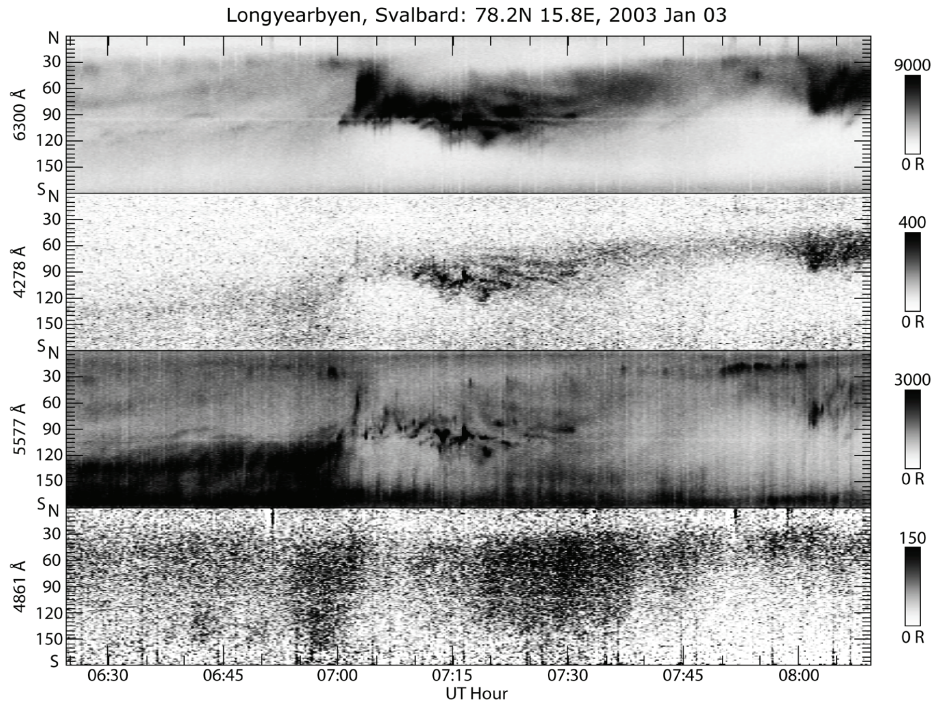

Figure 1. MSP keogram for January 3, 2003 from 0625 – 0810 UT. The four panels from top to bottom show emission intensity as a function of elevation angle in the magnetic meridian and time for the wavelengths 6300 Å [O I], 4278 Å N_2^+, 5577 Å [O I], and 4861 Å H_β. Intensity in Rayleighs is given in the colour scale.

Balmer emissions from neighboring spectra, are given in Sect. 2. Two case studies of simultaneous measurements at the sites are presented in Sect. 3. Interpretation of the proton energies derived from measurements at both locations is given in Sect. 4. Concluding remarks are given in Sect. 5.

2. Instrumentation and processing

2.1. Optical instruments

The two E-F spectrometers used in this study scan a wavelength region of nearly 80 Å about the two Balmer emissions. Each spectrometer consists of a spherical mirror, a reflecting grating at the mirror focus, curved entrance and exit slits, and a photomultiplier detector. For a particular position of the grating, the mirror images the entrance slit onto the exit slit at a particular wavelength.

The average linear dispersion, which is a measure of the width of a spectral interval

in the plane of the exit slit, is 3.06 Å/mm for the 1 m Green spectrometer at LYR and 4.18Å /mm for the ½ m Black spectrometer at NYA. Since the exit slit width for both instruments is 1 mm, the resulting bandpasses are 3.06 Å and 4.18 Å for LYR and NYA, respectively. Furthermore, due to the entrance and exit slits of both the spectrometers being matched, the bandpass in this case is identical to the full width at half maximum (FWHM) of the triangular instrumental function.

An order-sorting filter is placed before the entrance slit to prohibit overlapping spectral orders from contaminating the signal. Specifically, both instruments are measuring the second diffracted order. Spectral scanning is achieved by the mechanical rotation of the grating, driven by a synchronous motor. From the exit slit, a light pipe ducts the light to a thermoelectrically-cooled GaAs photomultiplier tube that has a nearly uniform spectral response across the wavelength region of interest. Both spectrometers have a field of view of 4-5 degrees along the entrance slit and are aligned to the local magnetic zenith, which is approximately 8 degrees south of geographic zenith in the magnetic meridian plane [*Sigernes et al*., 1996].

To allow the narrow-field spectrometer data to be interpreted in the larger context of auroral activity as a whole, data from the meridian scanning photometer (MSP) at Longyearbyen was used. This instrument is composed of a five channel photomultiplier array, each channel fitted with a narrow band interference filter which can be tilted relative to the optical axis. The tilting of the filters shifts the effective filter passband, thereby enabling background measurements in addition to peak measurements [*Romick*, 1976]. This is especially important to the measurement of emission lines with greatly varying backgrounds such as H_β.

The MSP photometers sweep the magnetic meridian via a scanning mirror with a full rotational period of 4 seconds. Data records are composed of two peak scans and two background scans, resulting in a time resolution of 16 seconds. In the current configuration, the MSP acquires data at the following peak wavelengths: 6300 Å [O I] ^{1}D, 4278 Å $N2^+$ 1NG, 5577 Å [O I] ^{1}S, 4861 Å H_β, and 8446 Å [O I]. With the Ny-Ålesund spectrometer located only 118 km from the MSP, there is sufficient overlap at E-region altitudes to use MSP keograms to determine if both of the spectrometers are recording hydrogen spectra from the same influx of protons.

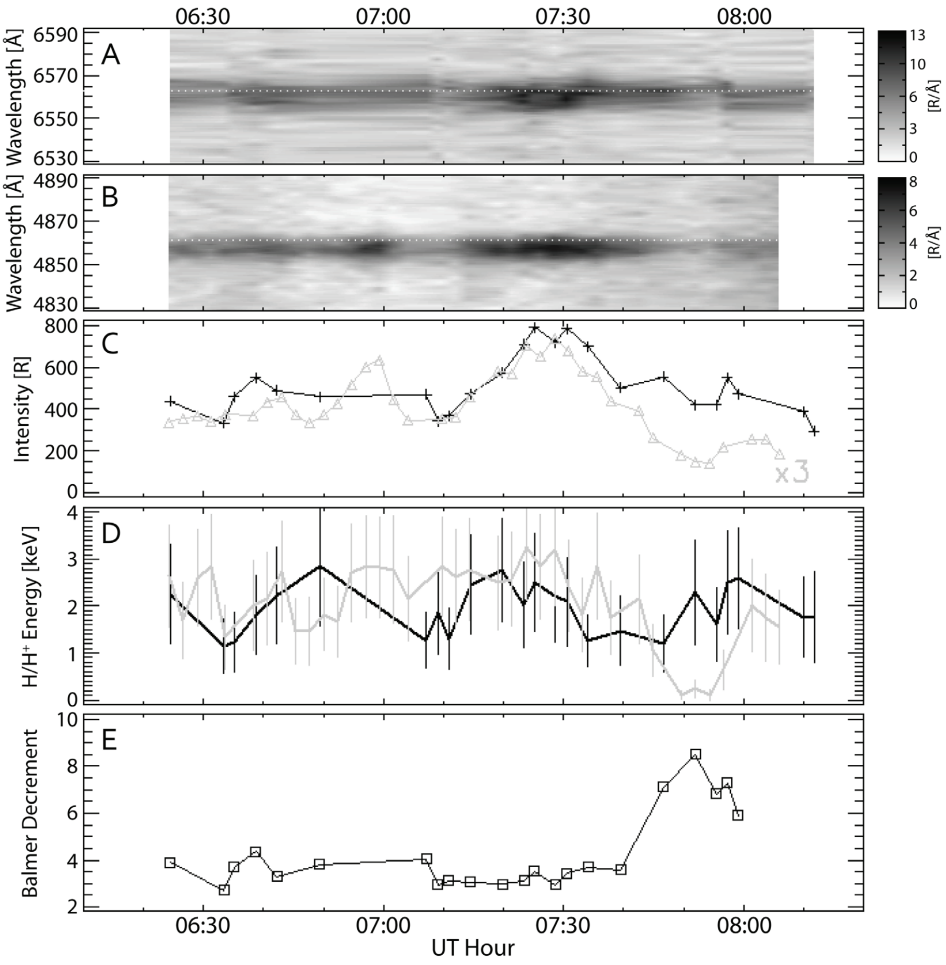

Figure 2. Time series of Balmer H_α and H_β spectra and derived parameters at Ny-Ålesund and Longyearbyen for January 3, 2003 between 0624 – 0812 UT. (A) H_α spectra, (B) H_β spectra, (C) integrated intensity: H_α (black), $H_\beta \times 3$ (grey), (D) fitted mean energy: H_α (black), H_β (grey), (E) Balmer decrement.

2.2. Data Processing

To improve the signal-to-noise (S/N) ratio of the Doppler profiles, two scans are averaged together. The two spectrometers have variations in design; for example, the 1 m E-F at LYR has a mirror focal length which is twice that of the 1/2 m E-F at NYA and the two scan at different rates. The spectrometer at NYA scans an additional wavelength region to observe the hydroxyl airglow layer after every H_α scan. Because of this, the minimum time required to acquire a profile of sufficient S/N is ~70 seconds for H_β at LYR and ~218 seconds for H_α at NYA. Both of the spectrometers are

calibrated absolutely with respect to intensity and wavelength using a scheme described in *Dyrland and Sigernes* [2007].

After the data are calibrated, spectral profiles for both emissions are corrected for variations in background and nearby emissions that can contaminate the signal. In the case of H_β, *Stringer* [1971] carefully studied the contamination of the Doppler profile by electron precipitation and found that the Vegard-Kaplan (2-15) band can contribute up to 25 % of the total signal, while the nearby O II lines possibly contribute up to 10 %. Methods for judging whether or not measured H_β intensities are contaminated by electron auroral emissions are discussed in *Moen et al.* [1998]. Electron auroral contamination of the H_β Doppler profile manifests itself as a varying background continuum brightness that must be subtracted [*Lummerzheim et al.*, 2003]. Also, near local noon on Svalbard, the affect of Rayleigh scattered sunlight must be accounted for [*Henriksen et al.*, 1985; *Robertson et al.*, 2006]. To correct for electron auroral contamination and Rayleigh scattered sunlight, an average normalized "twilight" spectrum, obtained during a period with no proton auroral emissions, is constructed. The normalization factor used is the average intensity in the wavelength region 4875-4915 Å. During the process of fitting an observed spectrum with the twilight spectrum plus the simulated Doppler spectrum, the twilight spectrum is scaled to account for varying solar zenith angle. This method is very similar to that applied to the H_α emission by *Borovkov et al.* [2005].

For the case of H_α, the removal of signal contaminants is more sophisticated. In order to isolate hydrogen emissions, neighboring spectra are simulated in order to be removed. Possible contaminants include the OH (6-1) airglow emissions and both the N_2 1PG (7,4) and N_2 1PG (6,3) electron auroral emissions at 6545- and 6624 Å, respectively [*Galand et al.*, 2004]. The relevant hydroxyl emissions were simulated using a procedure after *Sigernes et al.* [2003]. Then, the suitably normalized OH emissions were combined with a modeled H_α profile to provide a best fit to the measured data. For this study the OH spectral contaminants were simulated but the N_2 1PG emissions were not. Instead, MSP keograms were used to ensure that no significant electron auroral activity was simultaneously occurring.

The model profiles for H_α and H_β, assuming Maxwellian energy distribution in precipitated proton flux, are simulated from a library of profiles of varying initial energy. The library was produced by a series of Monte-Carlo simulations of proton precipitation, assuming a monoenergetic, isotropic initial proton beam in a dipolar

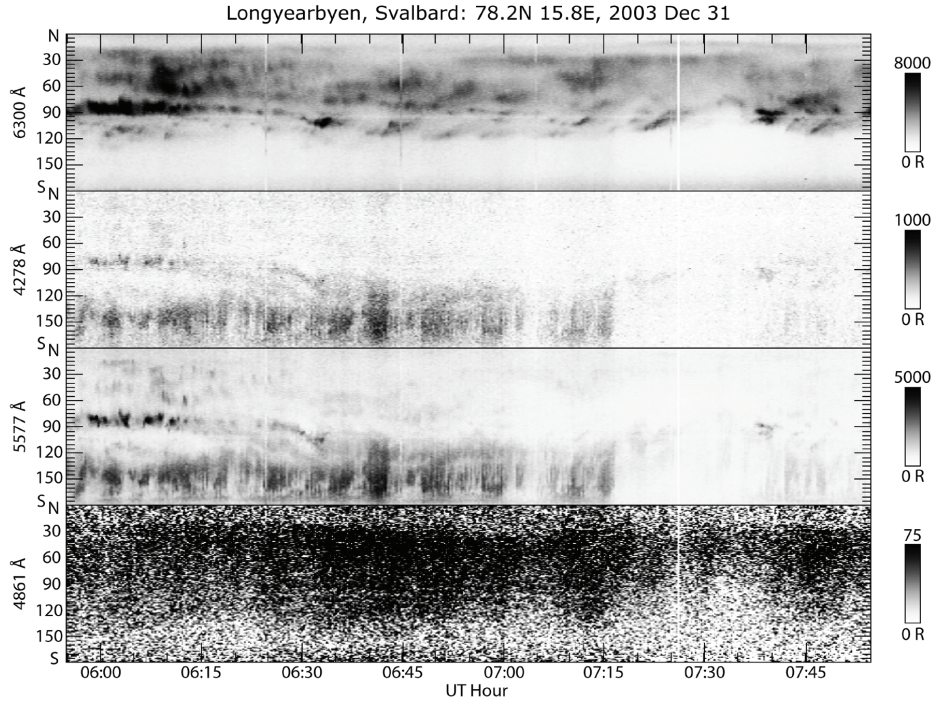

Figure 3. MSP keogram, similar to Figure 1, but for December 31, 2003 from 0555 – 0755 UT.

magnetic field. Furthermore, the hydrogen emissions produced are also assumed to be isotropic. The transport model was described in *Kozelov* [1993], *Kozelov and Ivanov* [1994], and *Kozelov and Kozelova* [1995], and was successfully applied to rocket [*Kozelov*, 1994] and ground-based observations [*Borovkov et al*., 2005]. In addition, this model accounts for unshifted geocoronal/galactic contribution, but not the red-shifted portion of the Doppler profiles.

3. Observations

We present two case studies found suitable to perform a proton energy analysis. The criteria used in data selection were the following: (1) Data acquisition at both locations was made under clear skies. Verification of sky conditions over Longyearbyen was made subjectively by inspection of channels of the MSP known to exhibit discrete arc activity, namely the 5577-, 4278-, and 8446 Å channels. At Ny-Ålesund the spectral time series of the 1/2 m Black spectrometer had to appear clean, meaning isolated from broadband emissions from the settlement backscattered by clouds. (2) Since both the H_α

and H_β signals can be contaminated by neighboring spectral emissions resulting from electron precipitation, all spectra must be compared with the 5577- and 4278 Å channels of the MSP to ensure minimal contamination. Also, the diffuse character of proton auroral emissions requires that they should appear as a relatively broad region in geomagnetic latitude, which can be verified by the H_β channel of the MSP at LYR.

3.1. January 3, 2003

Figure 1 shows the variation of auroral intensity with elevation angle and time (a keogram) from the meridian scanning photometer at LYR on January 3, 2003 from 0625-0810 UT. Note that magnetic noon is about 0850 UT for Svalbard. The panels from top to bottom indicate emissions at 6300-, 4278-, 5577-, and 4861 Å. We observed two bursts of proton precipitation, as shown in the H_β channel of the MSP, around 0655 UT and 0715 UT with durations of approximately 7 and 25 minutes, respectively. Note that between the two proton events there was a period of discrete electron aurora near geographic zenith at LYR, the implications of which will be discussed below. As seen from Longyearbyen, the bulk of the proton emission during both bursts was most intense between 40° and 120°, ensuring that the magnetic field-aligned spectrometer in Ny-Ålesund would observe the same proton events. Finally, the poleward edge of the proton emission in the keogram is well defined both during the proton bursts and outside of them. Beginning with the initial burst of 0655 UT, the poleward edge of the hydrogen emission region is seen to slowly drift poleward approximately 10 degrees by 0800 UT.

Spectra and derived parameters for the two spectrometers are presented in Figure 2. Note that the intensity scale of the H_α spectral time series (panel A) is larger than the H_β (panel B) below it. For the case of H_α, the intensity enhancement near 0715 UT is distinct, but the one at 0655 UT is not present since several spectra were unuseable. The H_β emission measured at Longyearbyen more closely follows the behavior of the corresponding MSP channel.

Panel C in Figure 2 shows the integrated intensity in Rayleighs for the two datasets. The wavelength integration limits are 6540-6575 Å for H_α and 4840-4875 Å for H_β. Again, the 0655 UT enhancement is visible in the H_β trace but not in H_α. The burst of hydrogen emissions beginning around 0715 UT peaks shortly before 0730 in both emissions. There are no significant time delayer between the two sites visible in the

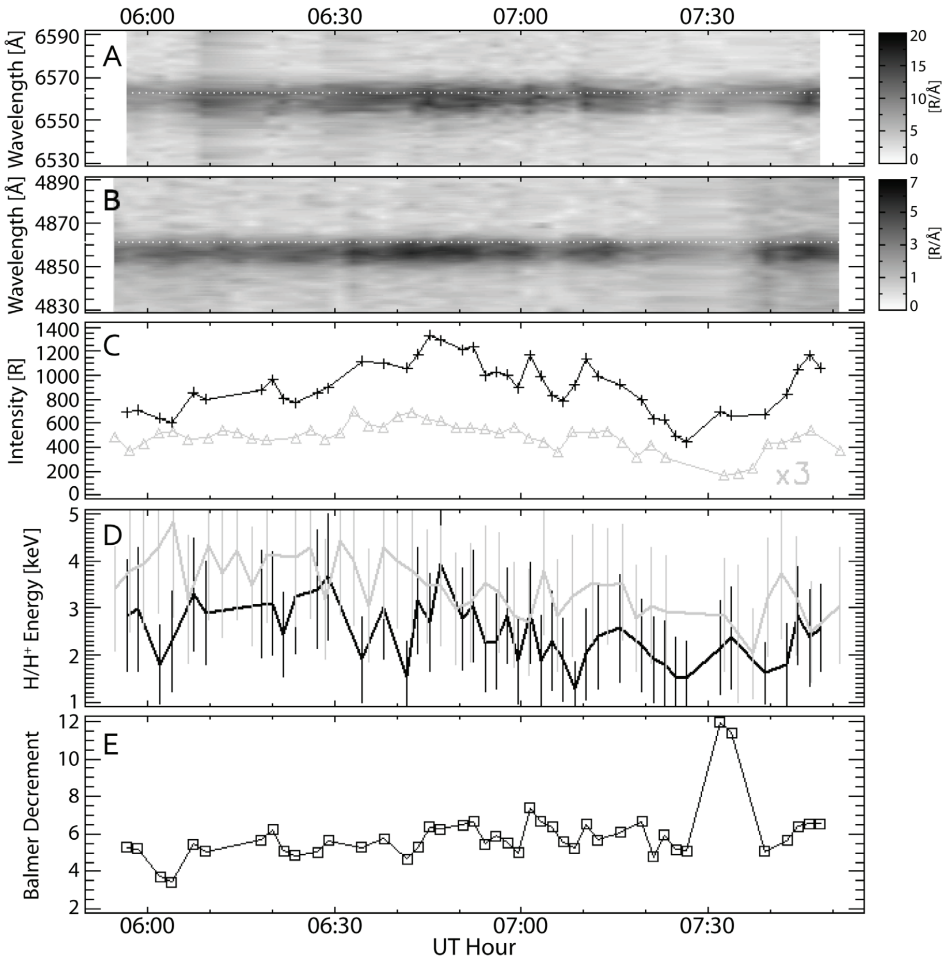

Figure 4. Balmer hydrogen emission time series, similar to Figure 2, but for December 31, 2003 from 0555 – 0755 UT.

data. Panel D shows the energy resulting from fitting a modeled Doppler profile to each spectrum. The scatter and uncertainty in the energy will be discussed below. The ratio of integrated intensities (panel C) is shown in panel E. For the time period, the Balmer decrement remains roughly constant until after 0740 UT where it increases sharply. Since there are more values of integrated intensity for H_β than for H_α, the ratio was only calculated at times for which H_α values were available.

3.2. December 31, 2003

The auroral dynamics for December 31, 2003 between 0555-0755 UT are characterized by the MSP in Figure 3. Like the previous case, this event occurred shortly before

magnetic noon at Svalbard. However, there exists more auroral activity over the time period than in the previous case. Specifically, equatorward of magnetic zenith over LYR, discrete aurora caused by electron precipitation dominates, as seen in both the 5577- and 4278 Å channels. The majority of the Balmer emissions occur mostly poleward of magnetic zenith at LYR, the most intense period being between 0630 and 0700 UT. In addition, inspection of the 6300 Å channel reveals both discrete features between 90° and 120° elevation angle and slightly more diffuse ones poleward of that. The brightness and character of the proton precipitation north of LYR eliminates the possibility that the diffuse red line emissions have been washed out owing to cloud cover; they are likely stimulated by secondary electrons produced in charge stripping collisions of the incident protons. Finally, note that the poleward edge of the hydrogen emission drifts slowly equatorward during the most intense period.

Figure 4 shows the hydrogen spectra measured at NYA and LYR for this case. Again, the intensity scale of the H_β plot is almost triple that of the H_α one. The enhanced period observed in the MSP H_β keogram between 0630 and 0700 UT is easily seen in panels A and C, as is an additional burst around 0740 UT.

4. Discussion

For the velocity filter effect to be observed, we expect a difference in the energy inferred from hydrogen Doppler profiles measured at LYR and NYA. Specifically, assuming poleward convection on the dayside, energy at LYR should be greater than that at NYA. Inspection of convection maps produced by the SuperDARN network of radars has shown that for both of the cases considered, on average, the ionospheric convection over Svalbard points from LYR towards NYA (not shown).

However, the uncertainties in the energy estimates in the Doppler profiles are such that for both cases, the error bars generally overlap. Thus, for a record-by-record comparison between the two locations, no significant energy difference is seen. The energy uncertainties are determined using a simple empirical estimation of total error that includes instrumental uncertainties and characteristics of the Doppler profile. Using the well-known relation between velocity and energy, the relative energy uncertainty can be expressed as:

$$\frac{E \pm dE}{E} = \frac{(v \pm dv)^2}{v^2} \tag{1}$$

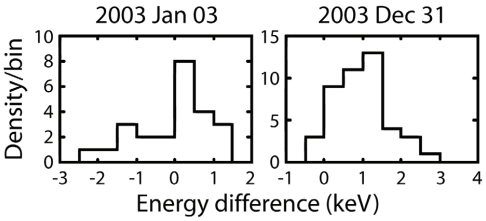

Figure 5. Distributions of energy difference ($E_p^{LYR} - E_p^{NYA}$) between Longyearbyen and Ny-Ålesund for both January 3 and December 31, 2003.

The uncertainty in the Doppler velocity, dv, is estimated by

$$dv = max(\frac{2dI}{I}, BP) \tag{2}$$

where I is the peak intensity of the profile, dI is the standard deviation of the error in the profile fit, v is the largest velocity in the profile above the noise floor, and BP is the instrument bandpass. For $dv/v = 1$, Equation 1 reduces to

$$\frac{dE}{E} = 2\frac{dv}{v} \tag{3}$$

Due to the instrumental bandpass of both of the spectrometers, Equation 2 is equal to that bandpass in the majority of cases. Thus the combination of large bandpass and low proton Doppler velocities associated with the cusp leads to the large and overlapping error bars in Figures 2 and 4.

Despite the fact that the large uncertainties in the energy estimates preclude us from comparing energies in a time-resolved fashion, for each case the energy separation can be treated in a statistical sense. Figure 5 shows distributions of energy differences ($E_p^{LYR} - E_p^{NYA}$) between the two stations for both cases considered. As was done with the Balmer decrement calculations, to determine energy differences, the H_β time series in panel D of Figures 2 and 4 was interpolated to the coarser H_α dataset. The percent of total samples whose difference was above 0 keV was 62.5- and 93.2 % for 03 January 2003 and 31 December 2003, respectively. Therefore for both of the cases, on average there is higher proton energy over Longyearbyen than Ny-Ålesund.

5. Conclusions

We have presented two examples of auroral hydrogen emissions over Svalbard and the inferred proton energy difference between Longyearbyen and Ny-Ålesund, which are

aligned along a geomagnetic meridian. Both cases have exhibited a separation in proton energy between the two stations, which supports the velocity filter effect paradigm. Unfortunately, the energy differences are only statistically significant after averaging over the entire time periods of interest (1h45m and 2h for 03 January and 31 December 2003, respectively). Distributions of energy difference were obtained; 62.5 and 93.2 % of samples in the distribution showed a positive energy difference, thus supporting the paradigm. Future work includes changing the instrumental configurations such that time-resolved, statistically significant measurements of proton energy can be interpreted in the context of dayside reconnection and ionospheric convection in and near the cusp.

Acknowledgements

The Auroral Station in Adventdalen is operated by The University Centre on Svalbard (UNIS) and owned by the University of Tromsø. The financial and operational support of the Space Physics and Aeronomy Group at the Geophysical Institute, University of Alaska Fairbanks, is sincerely appreciated. BVK was partly supported by the Russian Foundation for Basic Research (grant 06-05-65044), and by the Presidium of the Russian Academy of Sciences (RAS) through the basic research program "Solar activity and physical processes in the Sun-Earth system". CSD was supported by the National Science Foundation Atmospheric Sciences Section Grant No. ATM 0334800 to the Geophysical Institute of the University of Alaska Fairbanks.

References

Borovkov, L. P., B. V. Kozelov, L. S. Yevlashin, S. A. Chernouss (2005), Variation of auroral hydrogen emission near substorm onset, *Ann. Geo., 23*, 1623-1635.

Davidson, G. T. (1965), Expected spatial distribution of low-energy protons precipitated in the auroral zones, *J. Geophys. Res., 70*, 1061–1068, doi:10.1029/JZ070i005p01061.

Deehr, C. S., D. A. Lorentzen, F. Sigernes, and R. W. Smith (1998), Dayside auroral hydrogen emission as an aeronomic signature of magnetospheric boundary layer processes, *Geo. Res. Lett., 25*, 2111-2114.

Dyrland, M. E. and F. Sigernes (2007), An update on the hydroxyl airglow temperature record from the Auroral Station in Adventdalen, Svalbard (1980-2005), *Can J. Phys.*, 85, 143-151.

Eather, R. H. (1966), Red shift of auroral hydrogen profiles, *J. Geophys. Res., 71*, 5027.

Eather, R. H. (1967), Auroral proton precipitation and hydrogen emissions, *Rev. Geophys., 5*, 207-285.

Eather, R. H. (1988), Results from Antarctic optical studies, *Rev. Geophys., 26*, 579–590, doi:10.1029/RG026i003p00579.

Eather R. H. and F. Jacka (1966), Auroral hydrogen emission, *Aust. J. Phys., 19*, 241.

Fastie, W. (1952), A small plane grating monochromator, *J. Opt. Soc. Am., 42*, 641-647, doi:10.1364/JOSA.42.000641.

Galand, M., J. Lilensten, W. Kofman, and D. Lummerzheim. Proton transport model in the ionosphere (1998), 2. Influence of magnetic mirroring and collisions on the angular redistribution in a proton beam, *Ann. Geo., 16*, 1308.

Galand, M., J. Baumgardner, D. Pallamraju, S. Chakrabarti, U. P. Løvhaug, D. Lummerzheim, B. S. Lanchester, and M. H. Rees (2004), Spectral imaging of proton aurora and twilight at Tromsø, Norway, *J. Geophys. Res., 109*, A07305, doi:10.1029/2003JA010033.

Galand, M. and Chakrabarti, S. (2006), Proton aurora observed from the ground, *J. Atm. Sol. Terr. Phys., 68*, 1488-1501.

Galperin, Yu. I. (1959), Hydrogen emission and two types of auroral spectra, *Planet. Space Sci., 1*, 57-61, doi:10.1016/0032-0633(59)90025-X.

Haerendel, G. (1975), Die Spur der Magnetopause in Der Magnetosphäre, *Astron. Gesell. Mitt., 35*, 165-181.

Henriksen, K., N. I. Fedorova, G. F. Totunova, C. S. Deehr, G. J. Romick, G. G. Sivjee (1985), Hydrogen emissions in the polar cleft, *J. Atm. Terr. Phys., 47*, 1051-1056.

Kozelov, B. (1993), Influence of the dipolar magnetic field on transport of proton-H atom fluxes in the atmosphere, *Ann. Geo., 11*, 697-704.

Kozelov, B. V. (1994), Calculation of H_β emission in aurora. Comparison with observation, *Geomagn. Aehron., 34*(5), 86-90.

Kozelov, B. V., and V. E. Ivanov (1994), Effective energy loss per electron-ion pair in proton aurora, *Ann. Geophys., 12*, 1071-1075, doi:10.1007/s00585-994-1071-7.

Kozelov, B. V. and T. V. Kozelova (1995), Charge loss of proton flux as an additional source of plasma in F2 region, *Adv. Space Res., 16*(1), 159-162, doi:10.1016/0273-1177(95)00117-W.

Lanchester, B. S., D. Lummerzheim, M. H. Rees, M. Galand, J. Baumgardner, and F. Rich (2003), Proton and electron precipitation over Svalbard – first results from a new imaging spectrograph (HiTIES), Proc. of the 28th optical meeting, edited by K.

U. Kaila, J. R. T. Jussila, and H. Holma, *Sodankylä Geophysical Observatory Publications, 92*, 33-36.

Lorentzen, D. A. and J. Moen (2000), Auroral proton and electron signatures in the dayside aurora, *J. Geophys. Res., 105*, 12,733–12,745, doi:10.1029/1999JA900405.

Lummerzheim, D., and M. Galand (2001), The profile of the hydrogen H_β emission line in proton aurora, *J. Geophys. Res., 106*, 23–31, doi:10.1029/2000JA002014.

Lummerzheim, D., M. Galand, and M. Kubota (2003), Optical emissions from proton aurora, *Proc. of 28th annual optical meeting, edited by K. U. Kaila, J. R. T. Jussila and H. Holma, Sodankylä Geophysical Observatory Publications, 91*, 1-5.

McNeal, R. J. and J. H. Birely (1973), Laboratory studies of collision of energetic H^+ and hydrogen with atmospheric constituents, *Rev. Geophys. Space Phys., 11*, 633–692.

Meinel, A. B. (1951), Doppler-shifted auroral hydrogen emission, *Astrophys. J., 113*, 50-54.

Moen, J., D. A. Lorentzen, and F. Sigernes (1998), Dayside moving auroral forms and bursty proton auroral events in relation to particle boundaries observed by NOAA 12, *J. Geophys. Res., 103*(A7), 14,855–14,863, doi:10.1029/97JA02877.

Rees, M. H. (1982), On the interaction of auroral protons with the earth's atmosphere, Planetary and Space Science, *Planet. Space Sci., 30*, 463–472, doi:10.1016/0032-0633(82)90056-3.

Rees, M. H. (1989), Antarctic upper atmosphere investigations by optical methods, *Planet. Space Sci., 37*, 955-966.

Robertson, S. C., B. S. Lanchester, M. Galand, D. Lummerzheim, A. B. Stockton-Chalk, A. D. Aylward, I. Furniss, J. Baumgardner (2006), First ground-based optical analysis of H_β Doppler profiles close to local noon in the cusp, *Ann. Geo., 24*, 1-10.

Romick, G. J. (1976), The detection and study of the visible spectrum of the aurora and airglow, *Proc. Soc. Photo. Opt. Instrum. Eng., 91*, 63-70.

Rosenbauer, H., H. Grünwaldt, M. D. Montgomery, G. Paschmann, and N. Sckopke (1975), Heos 2 Plasma Observations in the Distant Polar Magnetosphere: The Plasma Mantle, *J. Geophys. Res., 80*, 2723–2737, doi:10.1029/JA080i019p02723.

Sigernes, F.; Fasel, L. G.; Minow, J.; Deehr, C. S.; Smith, R. W.; Lorentzen, D. A., Wetjen, L. T., Henriksen, K. (1996), Calculations and ground-based observations of pulsed proton events in the dayside aurora., *J. Atmos. Terr. Phys., 58*, 1281–1291.

Sigernes, F., N. Shumilov, C. S. Deehr, K. P. Nielsen, T. Svenøe, and O. Havnes (2003), Hydroxyl rotational temperature record from the auroral station in Adventdalen, Svalbard (78°N, 15°E), *J. Geophys. Res., 108*(A9), 1342, doi:10.1029/2001JA009023.

Sivjee, G. G.; Romick, G. J.; Rees, M. H. (1979), Intensity ratio and centre wavelengths of [O II] (7320-7330 Å) line emissions, *Astrophys. J., 229*, 432-438.

Stringer, W. J. (1971), Ph.D. thesis, University of Alaska Fairbanks.

Vegard, L. (1939), Hydrogen Showers in the Auroral Region, *Nature, 144*, 1089–1090, doi:10.1038/1441089b0.

Vegard, L. (1940), Continued investigations on the auroral luminescence and the upper atmosphere, *Geof. Publ., 14*, 16.

Yevlashin, L. S. (1961), Space-time variations of hydrogen in auroras and their connection with magnetic disturbances, *Geomagn. Aeron., 1*, 54-58.

Yevlashin, L. S. (2000), Hydrogen emission in auroras and the precipitation of auroral protons, *In: "Physics of the near-earth Space", part 3*, Apatity, Kola Science Centre RAS, 500–548.

Paper IV

The ion velocity filter effect observed in dayside hydrogen aurora

J. M. Holmes, B. V. Kozelov, N. J. Peters, C. S. Deehr, D. A. Lorentzen, F. Sigernes

Published in: Geophysical Research Letters

Citation: Holmes, J. M., B. V. Kozelov, N. J. Peters, C. S. Deehr, D. A. Lorentzen, and F. Sigernes (2009), Ion velocity filter effect observed in dayside hydrogen aurora, *Geophys. Res. Lett.*, 36, L23101, doi:10.1029/2009GL040972.

Paper V

Circumpolar ground-based optical measurements of proton and electron shock aurora

J. M. Holmes, M. G. Johnsen, C. S. Deehr, X.-Y. Zhou, and D. A. Lorentzen

Published in: Journal of Geophysical Research – Space Physics

Citation: Holmes, J. M., M. G. Johnsen, C. S. Deehr, X-Y. Zhou, and D. A. Lorentzen (2014), Circumpolar ground-based optical measurements of proton and electron shock aurora, *J. Geophys. Res. Space Physics, 119,* 3895–3914, doi:10.1002/2013JA019574.